**Title**
Functional Photonic Integrated Circuits and Their Applications



**Author**
Wan, Jingwei

**Publication Date**
2021

Peer reviewed|Thesis/dissertation

# Functional Photonic Integrated Circuits and Their Applications

By

Jingwei Wan

Thesis

Submitted in partial satisfaction of the requirements for the degree of

master's of science

in

Electrical and Computer Engineering

in the

Office of Graduate Studies

of the

University of California

Davis

Approved:

S.J. Ben Yoo, Chair

J. Sebastian Gomez-Diaz

William Putnam

Committee in Charge

2021

# Contents

# List of Figures

# Abstract

**Functional Photonic Integrated Circuits and Their Applications**

Optical communication systems are being widely deployed all around the world. One of the key techniques behind all these properties is wavelength division multiplexing/demultiplexing (WDM) [1]. To implement WDM systems in photonic integrated circuits, arrayed waveguide grating (AWG) plays an important role as the core device doing both the demultiplexing and routing functions of wavelength channels [2].

The working principles of AWG are discussed in detail in Chapter 2. Based on these properties, the workflow of determining all the geometric parameters needed for designing a low-loss functional AWG is presented in the second section in Chapter 2. To have an accurate estimation of the performance of the AWG being designed, the last section in Chapter 2 presents the flowchart showing how to build a fast and accurate AWG simulator using Gaussian approximation, Fourier Transform, and mode coupling theory. Apart from basic theories of AWG design, examples including traditional AWG router (AWGR) and some other fancy photonic integrated devices such as flat-top AWG, reflective AWG/AWGR, polarization-insensitive AWG are discussed in depth in Chapter 3. In Chapter 4, fabrication processes of SiN-based waveguide platform and measurement results of regular AWGs and reflective AWGs are described in detail. In Chapter 5, sophisticated system-level applications using AWGs including optical arbitrary waveform generator (OAWG), optical synaptic interconnections, and a passive part of WDM laser are introduced.

# Chapter 1

# Introduction

## 1.1 Silicon and Silicon Nitride Photonics

Thanks to the first demonstration of the semiconductor laser in 1962 [3] and the high-transmittance property of Silicon at the 1.3 $\mu$m and 1.55 $\mu$m fiber-optical wavelengths [4], integrated photonics on silicon platform has become an active area of research, especially in the optical communication area. To integrate with CMOS very large scale integration (VLSI), silicon photonics must be fabricated in a way compatible with multiple CMOS manufacturing techniques. One of the common platforms of silicon photonics widely used in optical communication devices is silicon-on-insulator (SOI) [5]. SOI wafer supports the fabrication of Si wire waveguides and Si slab waveguides. The refractive index of the Si core region is 3.480 and the $SiO_2$ cladding region is 1.444 at 1550 nm wavelength. The high index contrast provides a strong constraint for the optical mode propagating in the Si waveguide. As a result, the bending radius of Si waveguides can be as low as 2 $\mu$m for a 220 nm lightly p-doped Si core waveguide [6]) which means the footprint of Si-based photonic integrated devices can be very small. Also, the high core-cladding contrast makes the cross-section of a single mode waveguide relatively small (0.48 $\mu$m $\times$ 220 nm at 1550 nm wavelength). The disadvantage is that the small Si waveguide is highly sensitive to fabrication imperfections.

Silicon nitride ($Si_3N_4$) platform is a good substitute in terms of relatively low propagation loss and core-cladding index contrast [7]. The refractive index of the $Si_3N_4$ core is

2.00 and the $SiO_2$ cladding region is 1.444 at 1550 nm wavelength. For a 200 nm thick $Si_3N_4$ platform, the width of a single mode waveguide at 1550 nm is around 2 $\mu$m. The relatively large waveguide cross-section makes $Si_3N_4$-based devices less sensitive to fabrication imperfections. For some devices which are extremely sensitive to phase errors such as arrayed waveguide gratings (AWG), lower index contrast waveguide platform is more suitable. The disadvantage is that the relative weak constrain of mode requires the bending radius to be larger than 100 $\mu$m. In that case, Si-based devices are more compact compared with the $Si_3N_4$-based version.

## 1.2 Wavelength division multiplexing

In the spectrum of single mode optical fiber, there are two typical regions people are using in optical communication – original band (O-band from 1260 nm to 1360 nm) and conventional band (C-band from 1530 nm to 1565 nm). To maximize the data density in these two communication bands, each band is divided into multiple channels and each channel can only occupy a narrow range of wavelength. The smaller channel spacing is, the more channels can be utilized, and the greater the capacity of communication is. This technique is called wavelength division multiplexing. The device that can combine multiple channels on the same fiber or the same waveguide is a multiplexer. The device that can separate multiple channels into different spatial ports is called demultiplexer. Most of the time, a multiplexer can work as a demultiplexer if its inputs and outputs are swapped, and vice versa.

Arrayed waveguide grating (AWG) is a planar photonic device working as a de/multiplexer. The thesis further discusses versatile AWGs such as AWG routers (AWGR), flat-top AWGs, as well as some complex system-level applications.

# Chapter 2

# AWG principle, design, and simulation

## 2.1 AWG principle

An AWG is dispersive so it is widely used as a multiplexer and demultiplexer [8]. It can image the light from any input to any output based on different wavelengths as shown in Figure 2.1. A standard AWG consists of two star couplers and many arrayed waveguides as presented in Figure 2.2. A star coupler has single or multiple radiating apertures connected to input or output waveguides on the one side and multiple arrayed apertures connected to arrayed waveguides on the other side. The middle region of the star coupler is called free propagation region (FPR) which allows light propagating like in the free space. The arrayed apertures on the arrayed waveguide side capture the diffracted light. The arrayed waveguides have linear length differences ($\Delta L$) which can provide linear phase difference like a traditional grating.

## 2.2 AWG design

To design an AWG, these parameters need to be clarified by users: center wavelength ($\lambda_0$), channel spacing ($CS$), number of input and output ports ($N_{in}$ and $N_{out}$), FPR length ($f_1$ and $f_2$), input and output port width ($w_1$ and $w_2$), grating order ($m$), arrayed aperture spacing ($d_1$ and $d_2$), effective index of arrayed waveguides ($n_{eff}$), group index of arrayed waveguides ($n_g$), effective index of the FPR ($n_{slab}$). The rest parameters including


Figure 2.1. AWG imaging and dispersive principle. Lights with four different wavelengths coming from the input will be imaged on these four output ports based on their wavelengths.

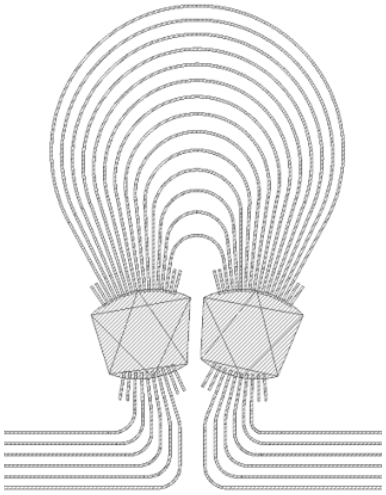

Figure 2.2. AWG schematic showing input waveguides, input star coupler, arrayed waveguides, output star coupler, and output waveguides

length different of arrayed waveguides ($\Delta L$), input and output spacing ($D_1$ and $D_2$), and propagation coefficient in the FPR ($\beta_s$) and in the arrayed waveguide ($\beta$), are determined by user-defined parameters. Some parameters are shown in Figure 2.3.

The most basic rule for an AWG to obey is the interference condition (Equation 2.1) [8]. To explain the meaning of each term in the equation, let us take Figure 2.3 for example. If two light beams are coming from the same input and focused on the same output but through two different paths (the $j$-th path and the $(j-1)$ -th path). To make sure these two waves are in phase, the phase difference must be an integer multiple of $2\pi$. The first term $\beta_s(\lambda)(\frac{d_1 x_1}{f_1})$ and the third term $-\beta(\lambda)(\frac{d_2 x_2}{f_2})$ in Equation 2.1 are the phase differences caused by the input star coupler and the output star coupler. The term in the

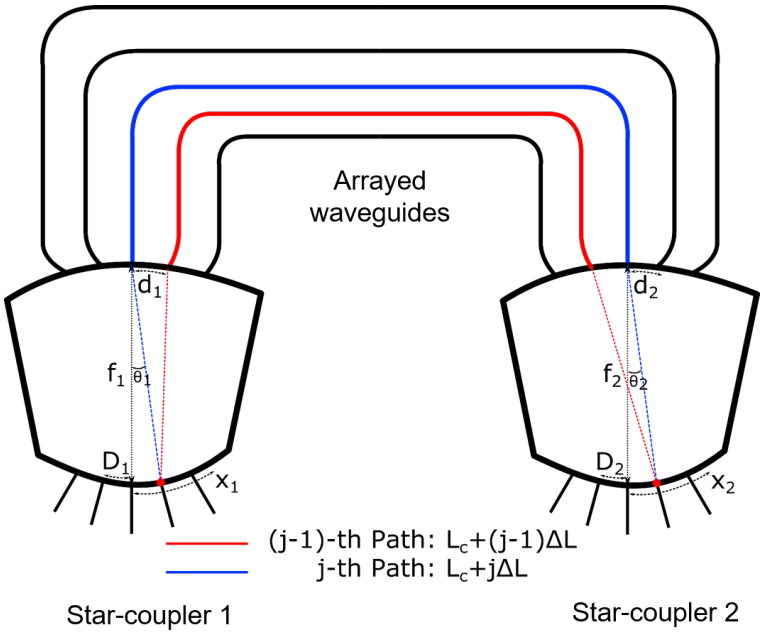


Figure 2.3. AWG design schematic with some important design parameters

middle $\beta_s(\lambda)\Delta L$ is caused by the length difference from the adjacent arrayed waveguides. $m$ is an integer called the "grating order".

$$\beta_s(\lambda)(\frac{d_1 x_1}{f_1}) + \beta(\lambda)\Delta L - \beta_s(\lambda)(\frac{d_2 x_2}{f_2}) = 2m\pi \tag{2.1}$$

For a light beam at the center wavelength coming from the center input ($x_1 = 0$), it must be focused on the center output ($x_1 = 0$). As a result, we can simplify the interference condition as below:

$$\beta(\lambda_0)\Delta L = 2m\pi \tag{2.2}$$

In Equation 2.2, $\Delta L$ is only dependent on the diffraction order $m$. Since $m$ will affect FSR as shown in Equation 2.3, $m$ can be either determined by a given FSR or can be a certain integer if FSR is not clearly defined.

$$m = [\frac{n_0\nu_0}{n_0\nu_0 - n_1\nu_1}] \tag{2.3}$$

$$\nu_1 = \nu_0 - \nu_{FSR} \tag{2.4}$$

To calculate the spatial dispersion of $x_1$ in Equation 2.1, we can take the derivative of Equation 2.1 with respect to $\lambda$.

$$\frac{dx_1}{d\lambda} = -\frac{n_g f_1 \Delta L}{n_s d_1 \lambda_0} \tag{2.5}$$

where $n_g$ is the group index of arrayed waveguides. Equation 2.6 indicates the relationship between the wavelength shift and the spatial dispersion of the focal point position $x$. If the wavelength shift $d\lambda = CS$, then the input gap $D$ is determined as

$$D_1 = -\frac{n_g f_1 \Delta L}{n_s d_1 \lambda_0} \times CS \tag{2.6}$$

In a real AWG, the first and the second star coupler always have the same geometric structure, which means we can define $D = D_1 = D_2$, $d = d_1 = d_2$, and $f = f_1 = f_2$.

$$D = -\frac{n_g f \Delta L}{n_s d \lambda_0} \times CS \tag{2.7}$$

For now, we have all the basic parameters needed to design an AWG. However, there is another problem with respect to topology – how to route the length-fixed arrayed waveguides without crossings. In Figure 2.4, three strategies are provided. In Figure 2.4 (a), the "circular" routing strategy is used. The advantage is that the bending radius is relatively large which means it is suitable for low-contrast waveguide materials. The disadvantage is that the large bending regions limit the size of AWGs. In Figure 2.4 (b), the "rectangular" routing strategy is used. All the bending regions have the same small bending radius and the same 90-degree bending angle. Compared with the "circular" routing strategy, the "rectangular" routing strategy require less area and the whole AWG can be fitted in a thin and long rectangle region. Also, the "rectangular" routing strategy can use multi-mode waveguides in straight regions to reduce phase error. One common disadvantage for both "circular" strategy and "rectangular" strategy is when FSR becomes too large and the required length difference of arrayed waveguides becomes too small, then these arrayed waveguides will come too close together. One solution is to use the Ω-shape routing strategy as shown in Figure 2.4 (c). The two extra bending regions are used to compensate for the redundant length difference caused by the center bending region.

The difficulty of the AWG arrayed waveguides routing problem comes from the requirement that all the arrayed waveguides must come from the output of the first star coupler and go to the input of the second star coupler. What if we use only one star coupler and then we just need to satisfy half of the requirement? Here comes the reflective AWG which will be discussed in Chapter 3.

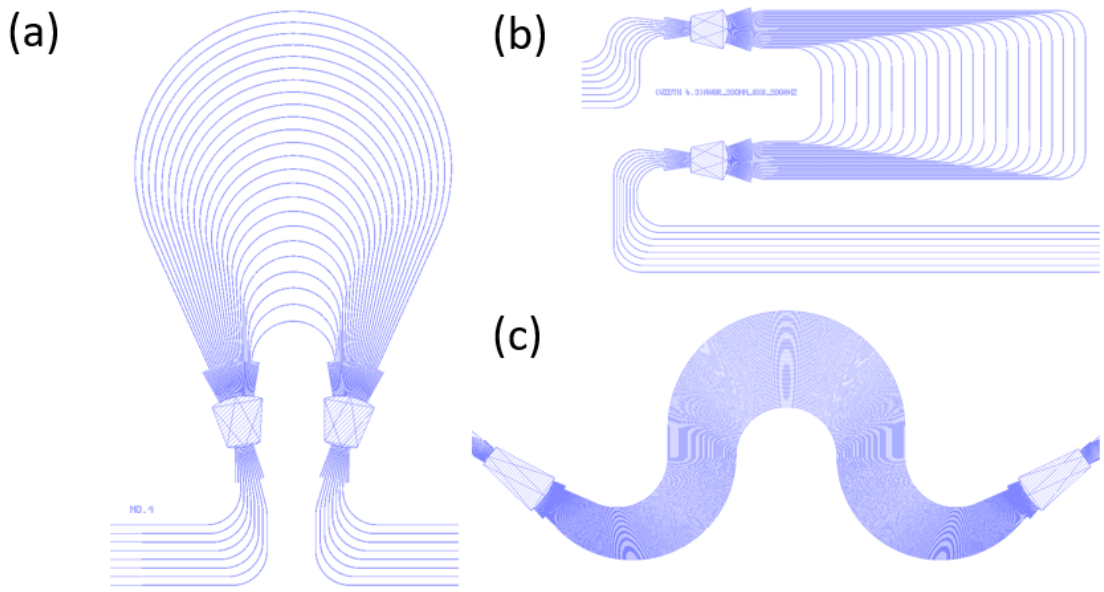


Figure 2.4. (a)AWG using the "circular" routing strategy. (b) AWG using the "rectangular" routing strategy. (c) AWG using the "Ω-shape" routing strategy.

## 2.3 AWG simulation

This section introduces the method to simulate the frequency response of an AWG. The main question of AWG simulation is how to simulate the light propagation in the star coupler or what we call the free propagation region (FPR). One common way is to use the beam propagation method (BPM) [9], but the calculation time highly depends on the size of the FPR. The larger the FPR is, the longer time it will take for the light to pass through. As a result, we can view the propagation as perfect Fraunhofer diffraction plus mode coupling [10]. Since the AWG is a planar device, we can simplify it again as a 1D propagating wavefront model. By doing that, the whole simulation time can be reduced to several minutes for a relatively high wavelength resolution.

As shown in Figure 2.5, the basic workflow to simulate a regular AWG is:

1. Generate a 1D Gaussian shape waveform as an approximation of the waveform at the input of the first star coupler. The width of the Gaussian wave is determined by the width of the eigenmode at the input aperture of the first star coupler. The eigenmode profile can be simulated by any simulation software such as Lumerical MODE solution and COMSOL.

2. Since the propagation mechanism in the FPR is viewed as Fraunhofer diffraction, it can be modeled by a Fourier Transform or a Fast Fourier Transform (FFT) in real implementations.

3. After the FFT, the electric field needs to be localized and coupled into those arrayed waveguides. The eigenmode of each arrayed waveguide is expressed in a Gaussian shape. After the mode coupling process, an extra phase shift will be attached to the electric field in each arrayed waveguide based on the length of the arrayed waveguide it belongs to. Then these localized fields are added together to form the field at the input of the second star coupler.

4. Similar to the first star coupler, the propagation in the second star coupler can be modeled using FFT.

5. The field after FFT is localized again and coupled into each output waveguide. We can obtain either the coupling coefficient or the waveform at the output waveguide.

For example, the AWG shown in Figure 2.6 is designed to be an 8x8 200 GHz channel spacing $Si_3N_4$ AWG with a 1280 nm center wavelength. Subplot (a) shows the electric field at the input of the first star coupler. The waveform has a narrow Gaussian shape. After FFT, the subplot (b) shows the electric field at the output of the first star coupler. The peak is broadened because of the Fraunhofer diffraction. Subplot (c) shows the electric field after propagating through the arrayed waveguides and at the input of the second star coupler. The previous waveform is sampled by these arrayed waveguides which accounts for these multiple small peaks but with the unchanged envelope. Subplot (d) shows the electric field at the output of the second star coupler. Actually, the output waveform is a combination of multiple images of the input waveform at multiple wavelengths. The

spacing between two adjacent peaks is an expression of frequency spectral range (FSR) in the space domain. Figure 2.7 shows the frequency response of the designed AWG in Figure 2.6.

The home-made AWG simulator is mainly programmed in Python, which makes it easier to maintain and update. However, because of the slow calculation speed of Python, the AWG simulator is not fast enough for iteration algorithm such as the gradient descent method (approximately 1 min for 800 frequency points on the commercial AMD 3600 CPU). As a result, the initial version of the AWG simulator has been rewritten in C++ by myself which has a 10x faster calculation speed. In that case, it is possible to be combined with machine learning algorithms in the future by my colleagues.

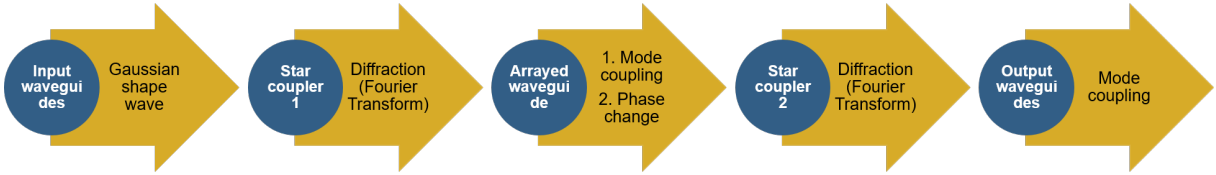


Figure 2.5. The flowchart of a regular AWG simulation

## 2.4 Conclusion

Starting from introducing the basic principle of AWG, we abstract the geometric model from an AWG. We separate the AWG model into several parts including the first star coupler, the second star coupler and the arrayed waveguides. Then the parameters needed to design an AWG are introduced. These parameters can be divided into two parts – self-defined parameters and calculated parameters. The processing of obtaining these calculated parameters are also shown in the chapter as well as three routing strategies. The next section shows the steps of building an AWG simulator using Gaussian beam approximation, Fourier Transform, and mode-coupling theory. Finally, an example of an $8 \times 8$ 200 GHz $Si_3N_4$ AWGR with center wavelength at 1280 nm is discussed.

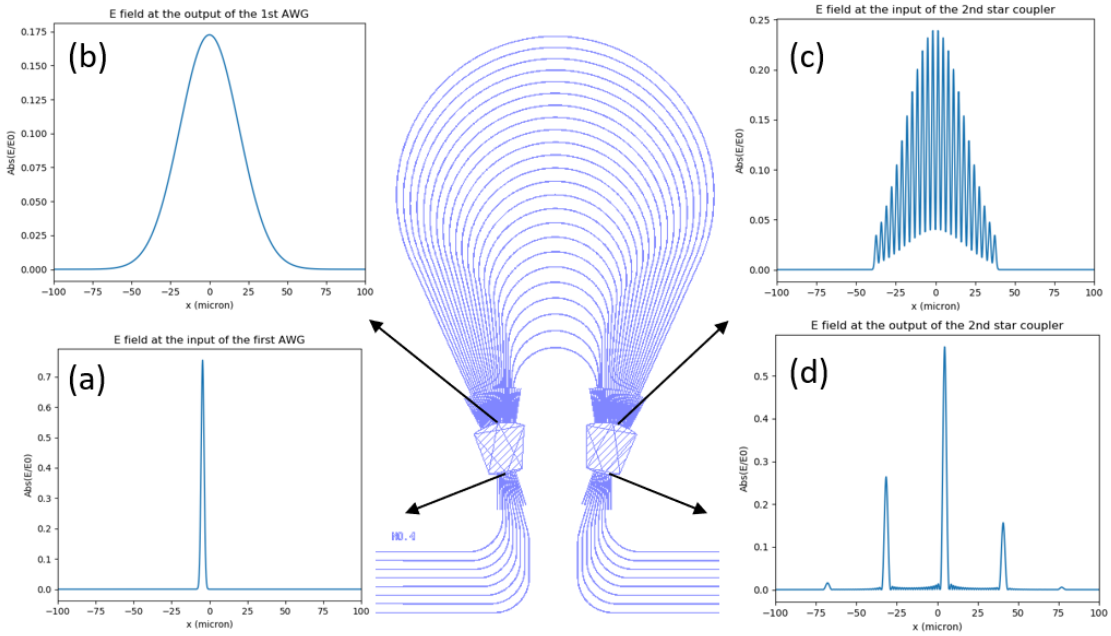


Figure 2.6. The electric field at 4 different positions of an 8x8 200 GHz channel spacing $Si_3N_4$ AWG. (a) The electric field at the input of the first star coupler. (b) The electric field at the output of the first star coupler. (c) The electric field at the input of the second star coupler. (d) The electric field at the second star coupler.

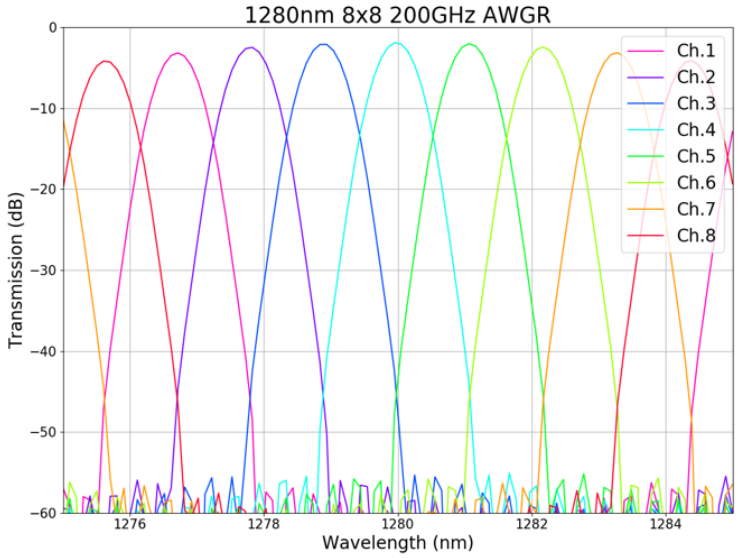


Figure 2.7. The corresponding frequency response of the 8x8 200 GHz channel spacing $Si_3N_4$ AWG in Figure 2.6

# Chapter 3

# Design examples

In this chapter, several examples of functional photonic devices will be introduced and discussed in detail.

## 3.1 Arrayed waveguide grating router (AWGR)

AWGR works as a router in an all-to-all optical interconnection system. The extension from AWG to AWGR was first proposed by Dragone [11]. A regular AWGR has $N$ inputs, $N$ outputs and it can route $N^2$ signals at the same time without mixing as shown in Figure 3.1. Figure 3.2 shows the difference between a regular AWG and an AWGR. Figure 3.2 (a) and Figure 3.2 (b) shows the property of a regular AWG, while (c) and (d) shows the property of an AWGR. Thanks to the cyclic property of AWGR, the spatial gap between the lowest channel within diffraction order $m$ and the highest channel within diffraction order $m-1$ is exactly equal to the spatial channel spacing ($D$ in Figure 2.3). As a result, the output ports of an AWGR can always capture all signals from all inputs as shown in (c) and (d). In the regular AWG, the output ports cannot always capture all signals as shown in (a) and (b).

To satisfy the cyclic property of an AWGR, the FSR needs to be finely controlled. From the study in Chapter 2, we know that FSR is highly dependent on the diffraction order $m$. The grating order $m$ is a self-defined value, which means we can choose the value of $m$ to satisfy the cyclic condition using Equation 3.1 and Equation 3.2.

$$m = [\frac{n_0\nu_0}{n_0\nu_0 - n_1\nu_1}] \tag{3.1}$$

$$\nu_1 = \nu_0 - \nu_{FSR} \tag{3.2}$$


Figure 3.1. AWGR schematic view showing the input and output mapping

$$m = [\frac{n_{eff}\nu_c}{n_g\nu_{FSR}}] \tag{3.3}$$

Here is an example of a 16x16 100 GHz channel spacing 200 nm thickness $Si_3N_4$ AWGR at the O band. The simulated results show high accuracy of the design tool (0.002% offset on the center wavelength and 0.09% offset on the channel spacing). Also, spectra in different diffraction orders are perfectly matched in a relatively large range (40 nm).

## 3.2 Flat-top AWG

A flat-top AWG is desirable because compared with the traditional Gaussian shape frequency response, it does not need a strict wavelength control in a communication network [12]. Also, in terms of working as the multiplexer in optical arbitrary waveform generator (OAWG) [13], the flat-top property is necessary to increase the passband.

Before going deep into the design of a flat-top AWG, we need to recall the mode overlapping in Chapter 2. The electric field of the eigenmode on a normal waveguide is in Gaussian-shape. If we can generate a double-peaks field, then we should be able to obtain a flat-top convolutional frequency response [14]. How to make sure the field at the

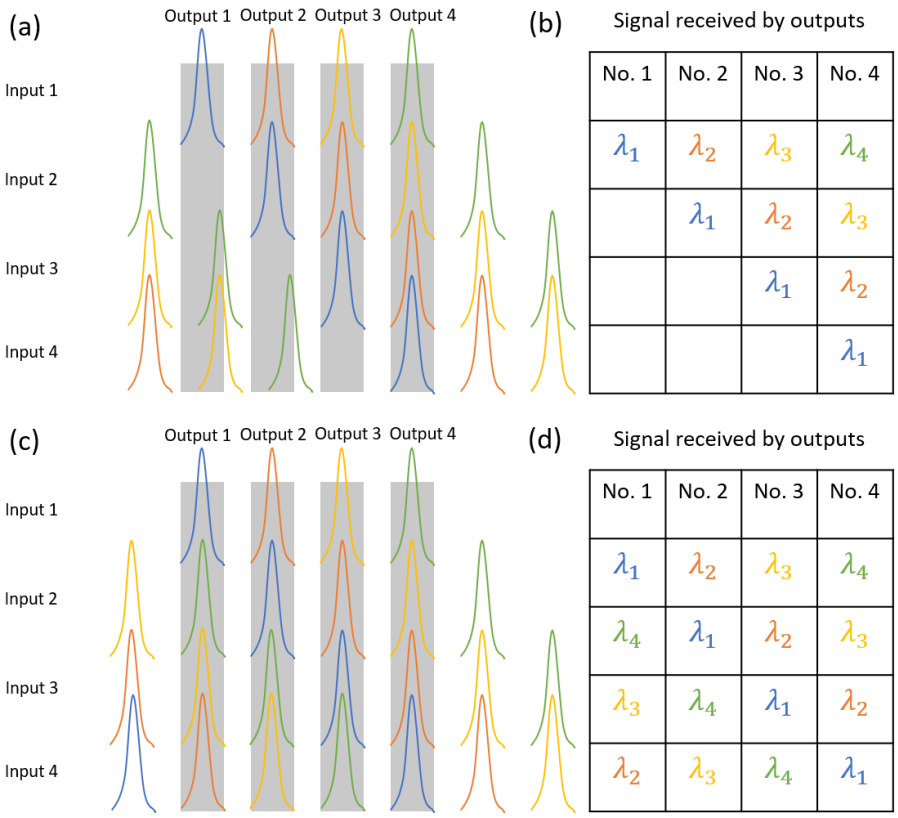


Figure 3.2. Comparison of AWG and AWGR. 16 singles comes from 4 different input ports loaded on 4 different wavelengths ($\lambda_1, \lambda_2, \lambda_3, \lambda_4$). (a) The electric field distribution schematic at the 4 outputs of a regular AWG. (b) The table shows the signals received by each output port of the regular AWG. (c) The electric field distribution schematic at the 4 outputs of an AWGR. (d) The table shows the signals received by each output port of the AWGR.

output of the second star coupler has a double-peaks shape? We need to use the imaging property of an AWG. If the input field is not a Gaussian shape but a double-peaks shape, then the field at the output of the second star coupler will also be in a double-peaks shape. When it is being coupled with the Gaussian shape eigenmode from the output waveguide, it is more possible to have a uniform coupling coefficient in a wide wavelength range (a flat-top response in the frequency domain) as shown in Figure 3.4. The next problem is how to generate a double-peaks waveform before the AWG and import it into the first star coupler.

There are multiple ways to achieve the double-peaks waveform such as using parabolic horn before the first star coupler [15], or multi-mode interferometer [16] or cascaded AWGs

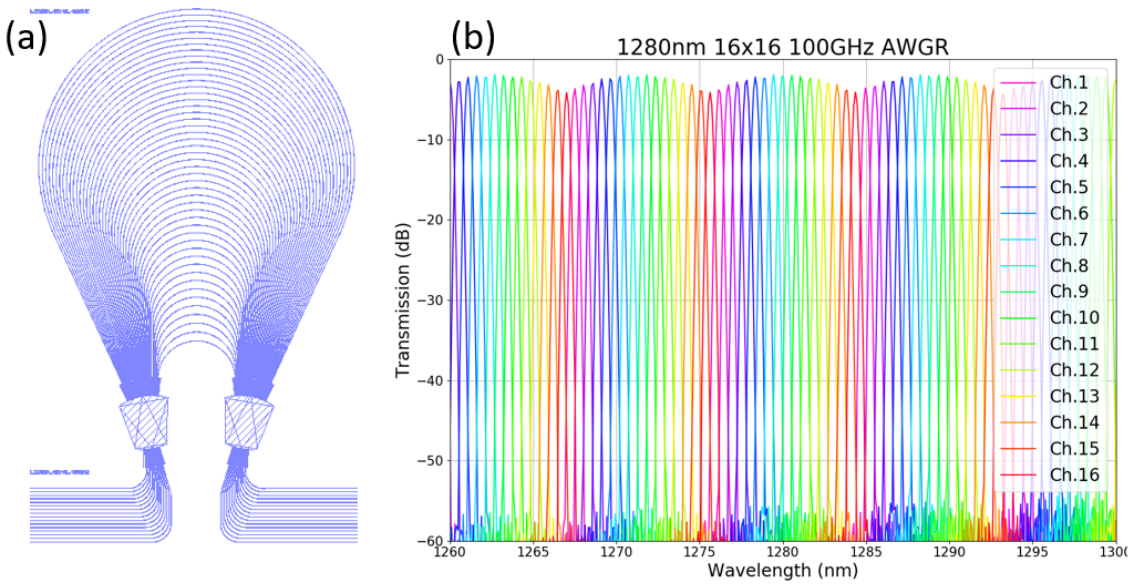


Figure 3.3. An example of 16x16 100 GHz channel spacing 200 nm thickness $Si_3N_4$ AWGR at O band. (a) The layout of the AWGR with a circular routing. (b) The overlaid 16 simulated spectra from the 16 outputs. Designed center wavelength is 1280 nm and the designed channel spacing is 100 GHz. The simulated center wavelength is 1279.98 nm with 0.002% offset; the simulated channel spacing is 99.91 GHz with 0.09% offset. The insertion loss is only 1.88 dB; crosstalk is less than -40 dB; 3dB-passband-cs ratio is 51.28%.

[17]. Our solution is the same as [16] by putting a multi-mode interferometer (MMI) as the input of the first star coupler as shown in Figure 3.4. In Figure 3.5, (a) shows the 2D electric field profile of a 3D FDTD simulation. We can choose the 1D electric field at any cutting line to be imported to the AWG simulator. We've tried various MMI width and MMI length to optimize the result. The MMI shown in (b) has a width of 4 $\mu$m and the length from the MMI input to the cutting line is 12.4 $\mu$m. After calculation, the output field of the second star coupler is shown in (a) in Figure 3.6. The depth of the middle hole decreases a little bit because of the coupling loss with the arrayed waveguides. Figure 3.6 (b) shows the frequency response of the flat-top AWG. Compared to the traditional AWG in Figure 2.7, the top is much flatter.

The flat-top AWG was fabricated by Guangyao Liu at UC Berkeley NanoLab on a 200 nm $Si_3N_4$ platform with center wavelength at 1291 nm and measured by myself. The measurement result is shown in Figure 3.7. (a) The simulated frequency response as

Figure 3.6 (b). The measured spectrum is shown in (b). Compared with the simulated spectrum, the center wavelength shifts about 1.0%; channel spacing shifts 1.9%; FSR shifts 4.6%. It is because of the index difference between the Lumerical database and the real $Si_3N_4$. Compared with the simulated spectrum, the measured spectrum has a higher 3 dB passband and higher loss. Because of the TM mode, the crosstalk at a lower wavelength is higher than the simulation result. The high sidelobes can be eliminated by controlling the polarization controller to reduce the TM component. Overall, the experiment result verifies the correctness of my flat-top AWG design.

According to the convolution model, the frequency response is not only related to the double-peaks field but also related to the Gaussian field. By controlling the width of the output aperture, we can control the width of the Gaussian field. As shown in Figure 3.8, output aperture width does make some differences. The narrower the aperture width is, the thinner the eigenmode field will be. Then it is harder to compensate the concave of the double-peak, which will generate the concave on the top of the spectrum.

## 3.3 Reflective AWG and AWGR

Reflective AWG is like a folded AWG with the same function but only occupying half of the space. The basic idea is to put reflectors at appropriate positions of the arrayed arms (still satisfying the interference conditions) and use the star coupler twice. As a result, a reflective AWG only has one star coupler, multiple shorter arrayed waveguides and reflectors as shown in Figure 3.9. Another advantage of reflective AWG is that the arrayed waveguides are not required to route from one star coupler to another star coupler. As long as these arrayed arms satisfy the length condition and not intersecting with others, they can be routed arbitrarily. In that case, we can optimize the space using spiral waveguides.

Compared with the reflective AWG, reflective AWGR has only one different thing – the definition of input and output. For a simple reflective AWG, only the first or the last several adjacent waveguides connected to the star coupler are called input waveguides and the rest of them are treated as output waveguides. Since input waveguides are all

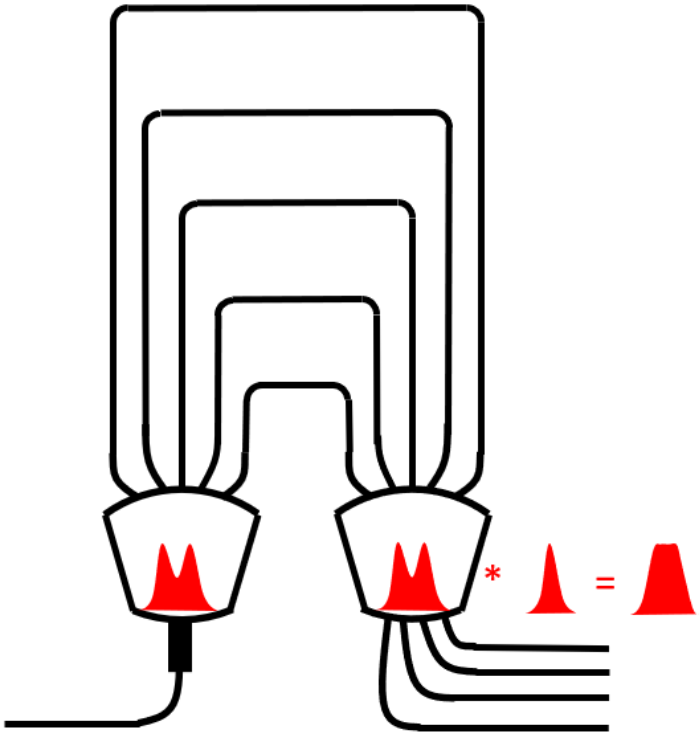


Figure 3.4. MMI AWG schematic diagram. The input MMI will generate the double-peaks shape field. The AWG will image it at the output of the star coupler. The double-peaks field will be coupled with the Gaussian-shape field belonging the output waveguide and generate a flat-top frequency response.

adjacent and output waveguides are also adjacent, there is no way to make the reflective AWGR a router. However, the reflective AWGR has interleaved input waveguides and output waveguides as shown in Figure 3.9 so it can work as a router.

Reflective AWGs have been demonstrated in the silica waveguide platform by L.G. de Peralta [18], the silicon waveguide platform using photonic crystal as reflectors by D. Dai [19] and the silicon nitride platform using Sagnac mirror as reflectors by Juan Fernández [20]. I have designed reflective AWGs using DBR from Mingye Fu as reflectors in silicon nitride platforms. The actual layout using PDK 4.0b from AIM Photonics is shown in Figure 3.10. It includes an 8x8 200 GHz channel spacing $Si_3N_4$ AWGR at the C band, Si thermal phase shifters, $Si_3N_4$ to Si couplers, $Si_3N_4$ to $Si_3N_4$ couplers and Si distributed Bragg reflectors (DBR). The $Si_3N_4$ AWGR and all the input waveguides are on the first $Si_3N_4$ layer when the output waveguides are on the second $Si_3N_4$ layer to avoid crossing.

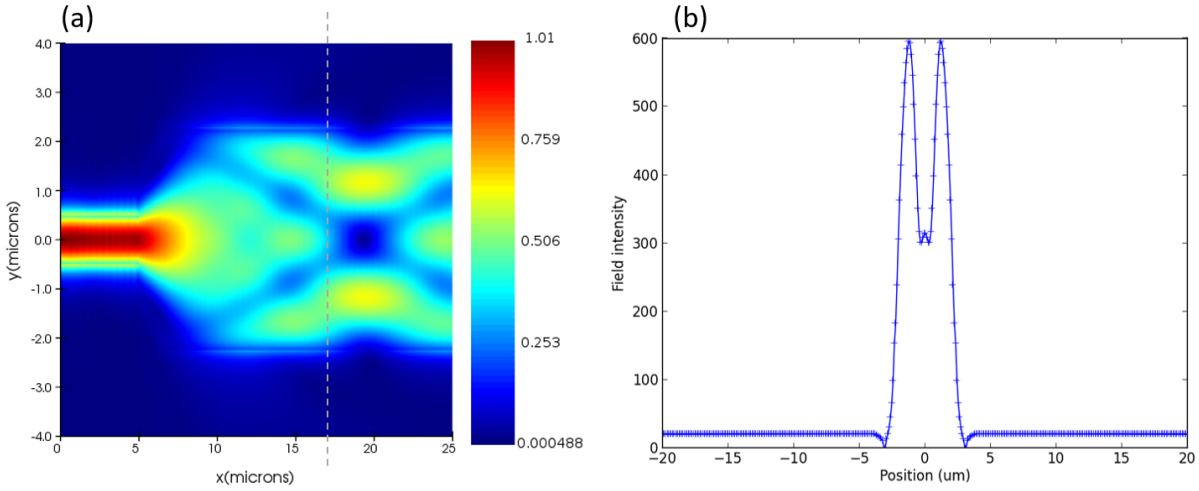


Figure 3.5. (a) FDTD simulation result of a 200 nm thickness $Si_3N_4$ MMI. The wavelength is 1291 nm; MMI input waveguide width is 1 micron; MMI width is 4 $\mu$m; MMI length is 25 micron; the distance from the beginning of the wide region to the cutting line is 12.4 micron. (b) The electric field at the cutting line shown in (a). This 1D electric field data will be imported as a self-defined electric field at the input of the first star coupler.

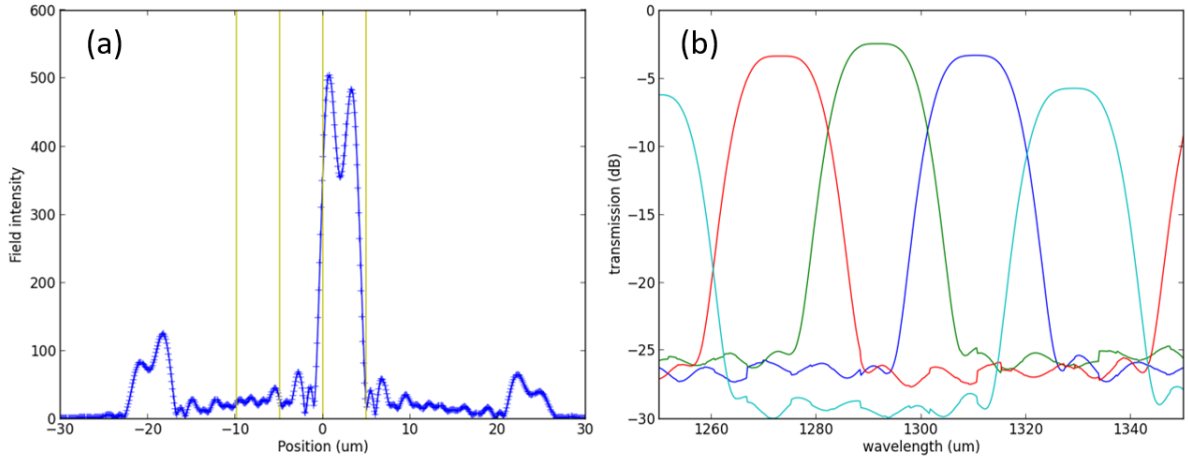


Figure 3.6. (a) The electric field at the output of the second star coupler. It still keeps the double-peaks shape. (b) The simulated frequency response from our home-made AWG simulator. The AWG is designed at 1291 nm; channel spacing is 3.5 THz.

At the end of each $Si_3N_4$ arrayed waveguide, a $Si_3N_4$ to Si coupler is utilized to couple light from $Si_3N_4$ layer to Si layer and tuned by the Si thermal phase shifters to reduce phase errors. After that, we put a Si DBR as a reflector in the end.

DBR reflectance is simulated using Lumerical 3D FDTD solution and the result is

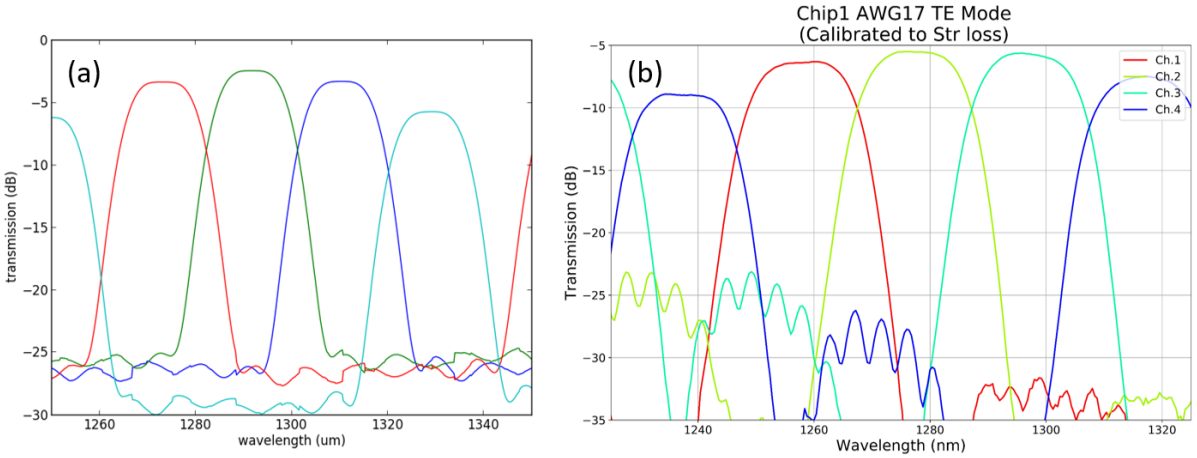


Figure 3.7. (a) The electric field at the output of the second star coupler. (b) The experiment result of the flat-top AWG. The measured center wavelength is 1277.4 nm (1.0% offset); the measured channel spacing is 3.567 GHz (1.9% offset); self crosstalk is -30.0 dB; 3dB passband channel spacing ratio is 51.44%.

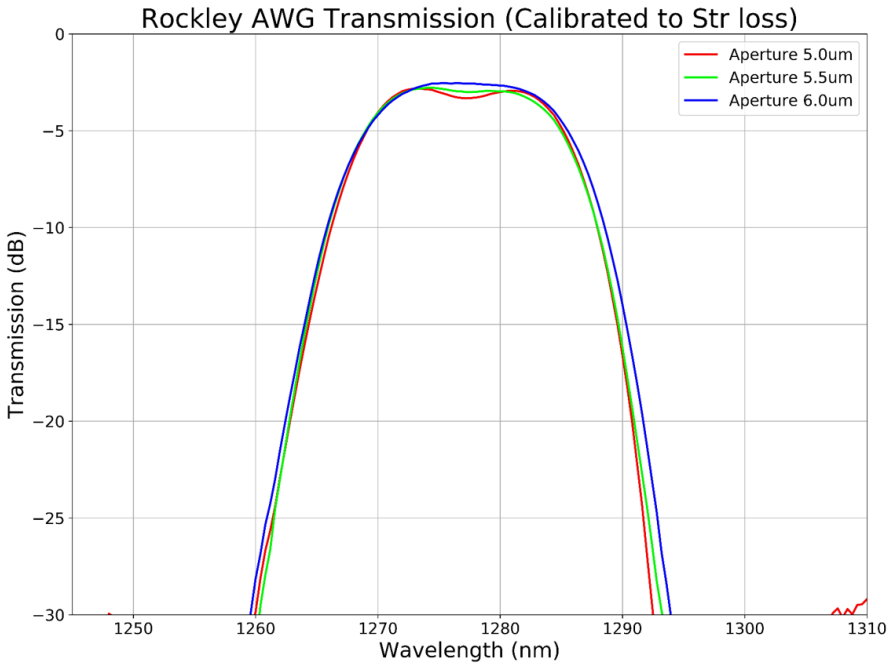


Figure 3.8. Experiment result: the frequency response of the flat-top AWG with different output aperture widths.

shown in Figure 3.11 (a). In the real tapeout, DBR with 10 grating periods is used ($N = 10$). In a wavelength range (from 1400 nm to 1650 nm) much larger than AWG working wavelength range (from 1530 nm to 1570 nm), the reflectance keeps on a high level (higher than 80%), which guarantees relatively good performance even if center wave-

length shifting happens because of fabrication error. To maximize the extinction ratio, AWG uses a conservative design which means the input and output apertures are designed to be wide enough to capture more light. Fabrication processes and measurements results are shown in the next chapter.

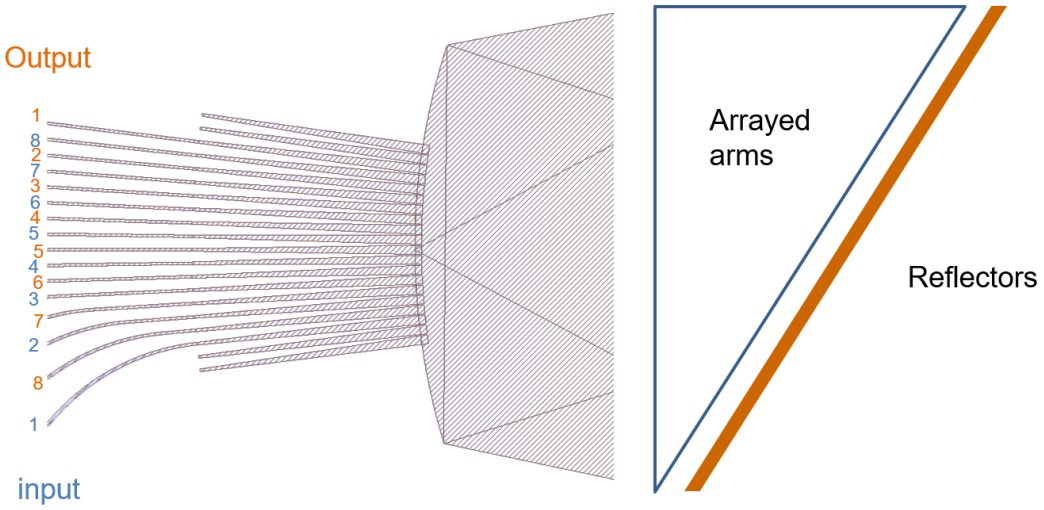


Figure 3.9. The schematic view of a reflective AWGR. The star coupler has 16 connected waveguides. Half of them are used as inputs and the rest of them are treated as outputs. Input waveguides and output waveguides must be interleaved as shown here to make it work like an 8x8 router.

## 3.4 Polarization-insensitive AWG

Since TE and TM mode has a different effective index on arrayed waveguides, there are center wavelength shifts for TE and TM modes in an AWG. To compensate for the phase difference, a special design of the star coupler is used [21]. In this design, the length of FPR region changes with the position of arrayed waveguides. The FPR length difference is used to compensate for the phase difference of TE and TM mode coming from the effective index difference on arrayed waveguides.

AWG grating equation:

$$2n_s\Delta L_s + n_a\Delta L = m\lambda_c \tag{3.4}$$

Consider TE and TM dispersion:

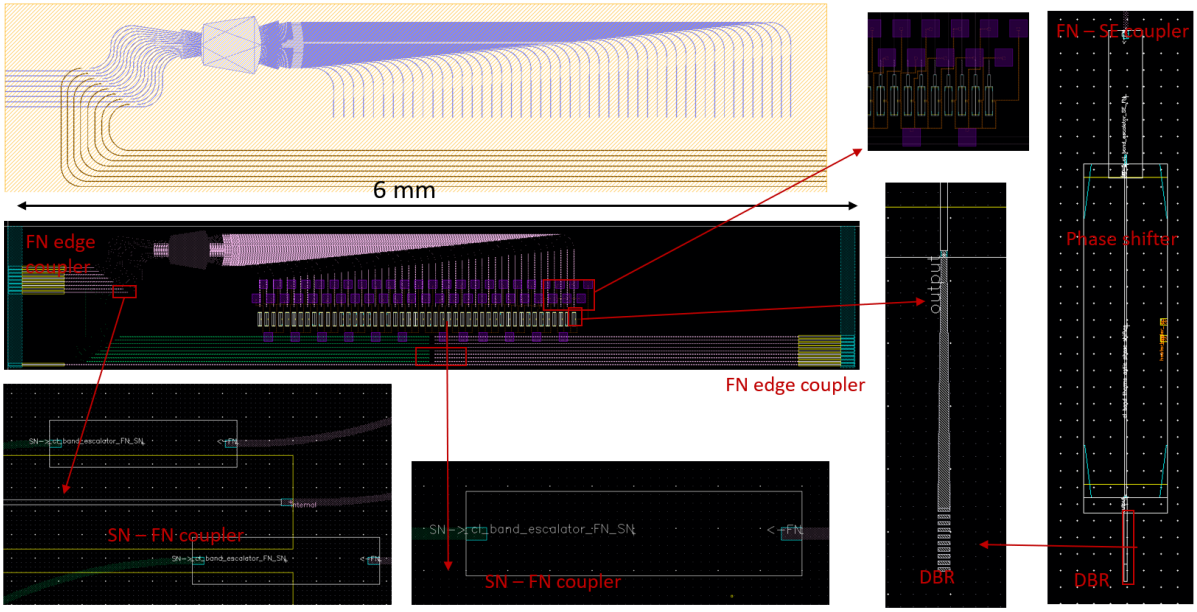


Figure 3.10. The layout of a tunable reflective AWGR using AIM Photonics PDK. The reflective AWGR is designed to be an 8x8 200 GHz channel spacing $Si_3N_4$ AWGR at the C band. The $Si_3N_4$ AWGR with input waveguides are on the first $Si_3N_4$ layer and the output waveguides are coupled into the second $Si_3N_4$ layer to avoid crossing. At the end of each arrayed waveguide, there is a thermal phase shifter to reduce phase errors. After the thermal phase shifter, a high-reflectance Si distributed Bragg reflector (DBR) covering the whole working wavelength range is used as a reflector.

$$\Delta\lambda = \lambda_{TE} - \lambda_{TM} = [\frac{2\Delta n_s \Delta L_s + \Delta n_a \Delta L}{2n_s \Delta L_s + n_a \Delta L}]\lambda_c \tag{3.5}$$

No dispersion condition:

$$2\Delta n_s \Delta L_s + \Delta n_a \Delta L = 0 \tag{3.6}$$

Then we can obtain the value of FPR length difference:

$$\Delta L_s = -\frac{\Delta n_a \Delta L}{2\Delta n_s} \tag{3.7}$$

The design and layout program is written by myself. Figure 3.12 shows the geometric diagram of the special star coupler. Figure 3.13 shows different star couplers when we have different birefringence values on arrayed waveguides.

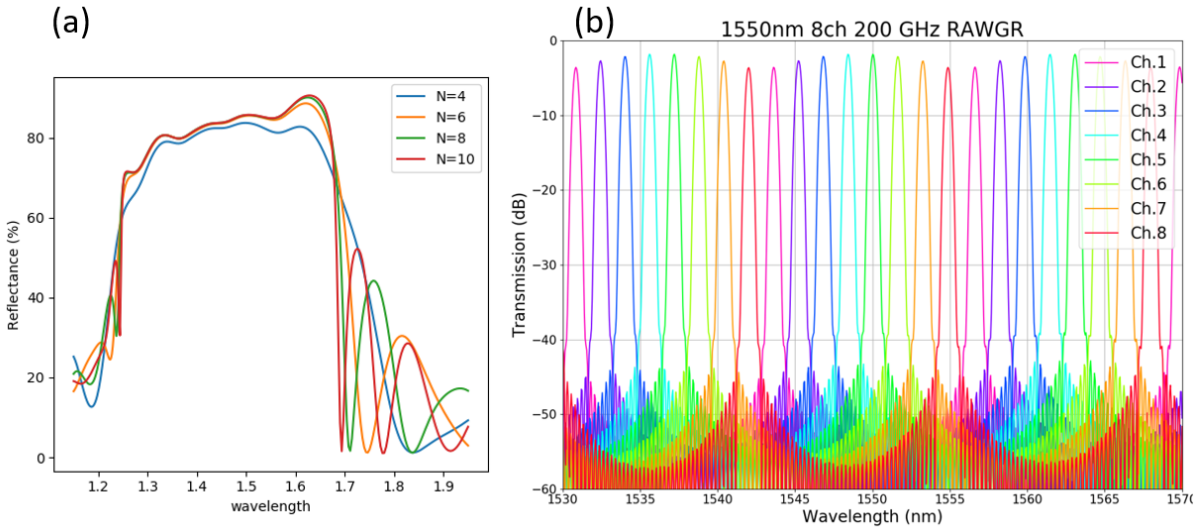


Figure 3.11. (a) The simulated spectra of the DBR with different N. The reflectance in the AWG working wavelength range is around 80%. (b) The simulated spectra of the reflective AWGR. Center wavelength is 1550.04 nm (0.0025% offset); insertion loss is 1.87 dB; channel spacing is 200.55 GHz (0.27% offset); crosstalk is less than -40 dB; 3 dB passband channel spacing ratio is 22.4%.

## 3.5 Conclusion

In this chapter, we go through 4 design examples of special AWGs including AWGR, flat-top AWG, reflective AWG, and polarization-insensitive AWG. AWGR works as a router in an all-to-all optical interconnection system. The design process of AWGRs has been well-developed. $8 \times 8$ AWGR and $16 \times 16$ AWGR fabrication and measurement results will be discussed in detail in the next chapeter. Flat-top AWG has a flat-top frequency response make it not sensitive to center wavelength offset. Some flat-top AWGs have been fabricated in Berkeley NanoLab and tested to be workable. The reflective AWG/AWGR is a combination of half of an AWG and multiple reflectors but still working as an AWG/AWGR. It will be fabricated by AIM Photonics. Polarization insentive AWG uses special design in the star coupler to compensate for the birefringence happening in the arrayed waveguides.

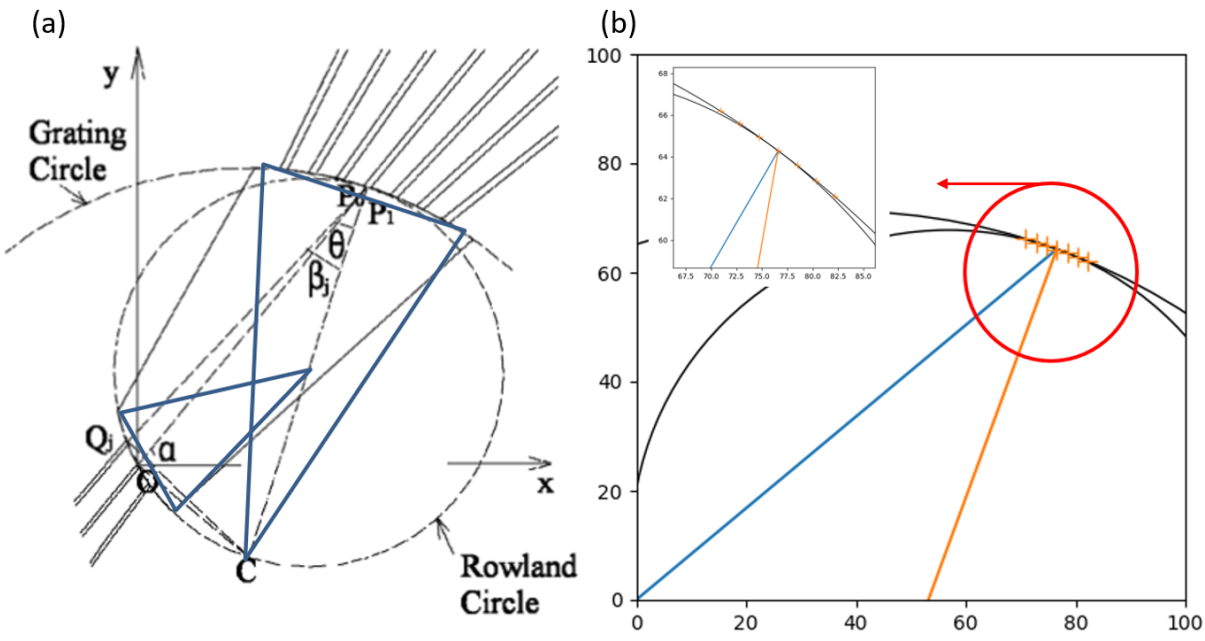


Figure 3.12. (a) Schematic diagram of the birefringence compensated input star coupler [21] (b) Implementation of the method in Python. Orange crosses show the positions of arrayed apertures.

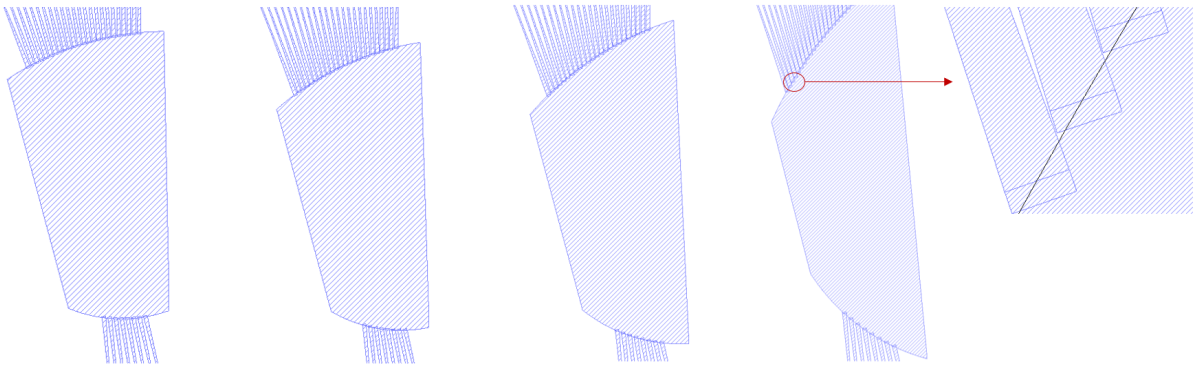

$\Delta n_a = -0.002$ $\Delta n_a = -0.004$ $\Delta n_a = -0.006$ $\Delta n_a = -0.01$

Figure 3.13. When birefringence on arrayed waveguides changes, the shape of star coupler will change, too. If the effective index birefringence is too large as shown in the last subplot, there will not be enough room to put many arrayed waveguides.

# Chapter 4

# Fabrication and measurement

## 4.1 Single-layer SiN waveguide platform fabrication

SiN waveguide platform is popular in the integrated photonics area thanks to its CMOS compatibility. This section summarizes a well-developed single-layer SiN waveguide platform fabrication process flow used in my AWG fabrication. All processes are completed in the UC Berkeley Marvell nanofabrication laboratory and the UC Davis Center for Nano-MicroManufacturing.

The process flow is shown in Figure 4.1. (a) The fabrication starts with a 6 micrometer-thick thermal oxide wafer with Si substrate. (b) The wafer is deposited with a thin SiN layer using LPCVD. The normal thickness we use is 150 nm or 200 nm. (c) 80 nm of amorphous Si is deposited on the top of the wafer as a hard mask using LPCVD. (d) The wafer is then coated with a bottom anti-reflection coating (BARC) layer to reduce reflectivity as resist interfaces and provide better linewidth control. (e) 430 nm photoresist layer is coated on the top of the wafer. (f) The wafer is exposed in the ASML DUV stepper. The achievable minimum feature size is 250 nm, which explains why the minimum gap in my AWG design is 250 nm. After the exposure, the wafer is developed in the developer and post-baked in the oven. The patterned photoresist layer is shown in Figure 4.2 (g) The BARC layer cannot be developed so it needs to be etched in a high frequency inductively coupled plasma (ICP) etch system. (h) After the BARC etching, the 80 nm amorphous Si layer is etched with a TCP etcher. (i) The remaining photoresist and BARC layers are

completely stripped using the matrix asher. Only the amorphous Si layer works as the hard mask. (j) The exposed part of 150 nm or 200 nm SiN layer is completed etched in the ICP etch system. The remaining SiN forms all the waveguides and AWG. After ICP etching, the wafer needs 45-second heated phosphorus etching to remove polymer that may attach to the waveguide. (k) Because the SiN layer needs to be buried in the SiO2 cladding, the amorphous Si hard mask can be thermal oxidized into a top cladding. (l) The rest cladding is formed with SiO2 deposition using LPCVD. The cladding thickness should be larger than 3.5 $\mu m$. The last step is to dice the whole wafer into many 10 mm x 5 mm dies. The diced chips are shown in Figure 4.3.

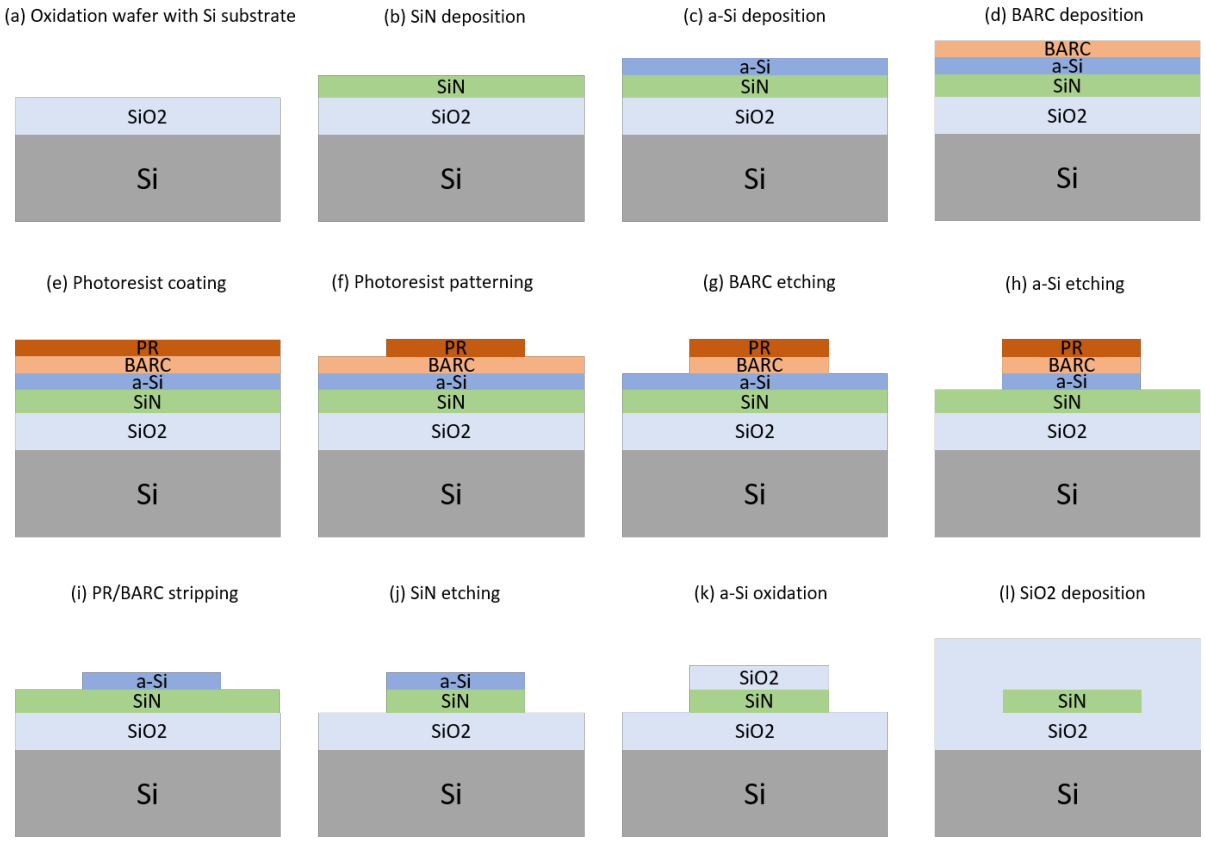


Figure 4.1. SiN waveguide platform fabrication process flow

## 4.2 AWGR measurement

The AWGR measurement setup is shown in Figure 4.4 and Figure 4.5. The light source is the amplified spontaneous emission (ASE) light source. It is connected with a single-

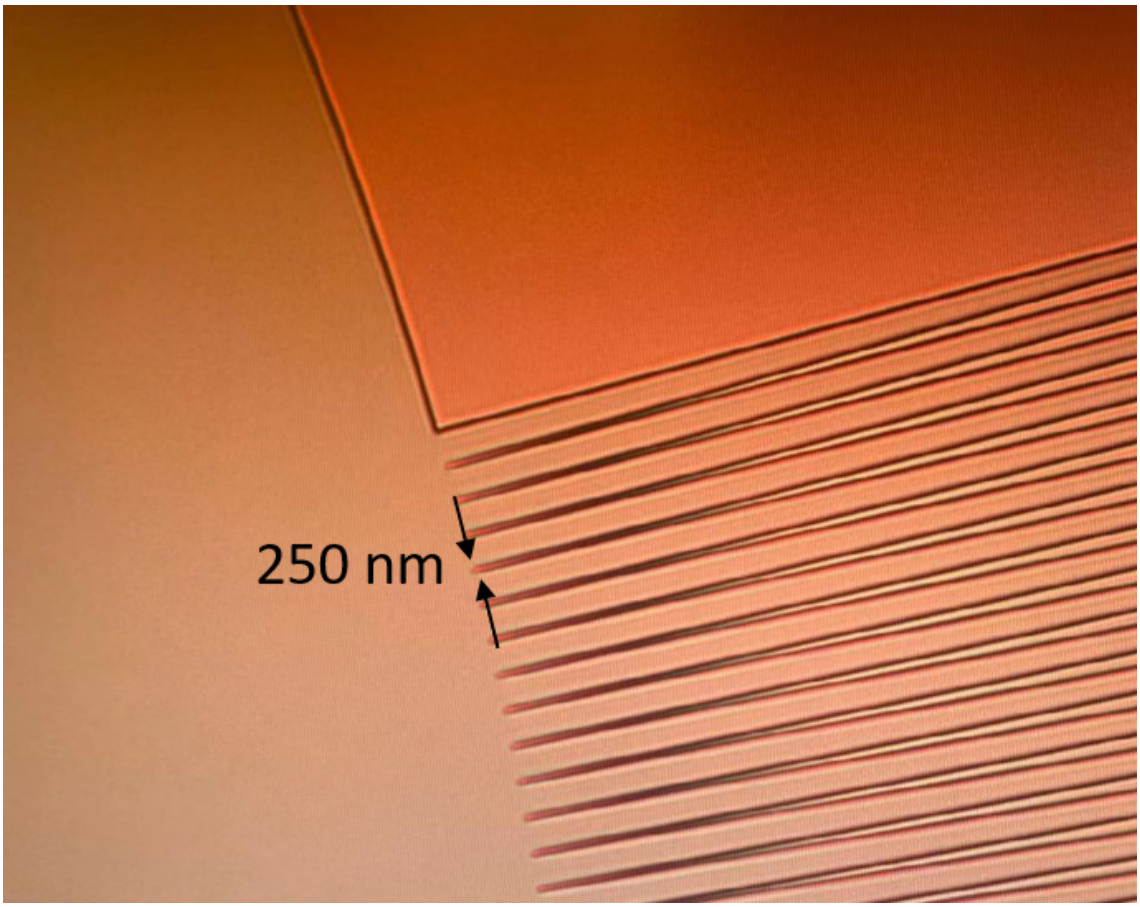


Figure 4.2. The photo shows the patterned photoresist layer after developing. The minimum aperture gap in AWG is 250 nm as shown in the figure above. It is decided by the minimum resolution of the stepper.

mode fiber and a polarization controller (PC). The PC is used to tune the polarization of the input light. The PC is then connected to a lensed fiber through a polarization-maintaining (PM) fiber. The lensed fiber is used to couple the input light into the chip under testing. The output light is coupled into another lensed fiber and finally goes into an optical spectrum analyzer (OSA).

The first tested AWG is an 8x8 200 GHz channel-spacing circular-shaped AWGR. The measured spectra are shown in Figure 4.6. Another test AWG is a 16x16 80 GHz channel-spacing box-shaped AWGR. They are fabricated by me together with Xian Xiao and tested by myself. The measured spectra are shown in Figure 4.7. All AWGs are fabricated using the 200 nm SiN waveguide platform process flow introduced in the previous section. Comparing these two spectra, we can see that AWGRs have very uniform

Figure 4.3. The chip size is 10 mm x 5 mm. The 2 chips on the left have 4 circular-routed 16x16 AWGRs. The two chips on the right have 4 8x8 AWGRs (small) and 4 16x16 AWGRs (large).

channel distribution and periodic insertion loss (about 3 dB roll-off), which agrees with the AWG design theory and simulation. The center wavelength offset and channel spacing offset possibly come from the error of effective index calculation. The relatively high crosstalk values are possibly a result of the phase error caused by the nonuniform arrayed waveguide width.

To investigate the influence of different input/output port widths, 3 AWGRs with different input/output waveguide port widths are measured. The results are shown in the Figure 4.8. The port width controls the passband width. The wider the port is, the wider the passband is. Another important concept is the crosstalk. Crosstalk consists of two parts, the adjacent crosstalk and nonadjacent crosstalk. When two adjacent channels are too close, adjacent crosstalk will dominate as shown in the first subplot in Figure 4.8. When two adjacent channels are not too close compared with their passband, the adjacent crosstalk will be similar to nonadjacent crosstalk. As a result, in order to avoid large adjacent crosstalk, an appropriate choice of input/output port width is important.

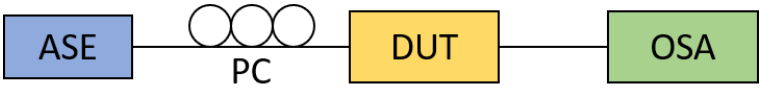


Figure 4.4. Measurement setup schematic view

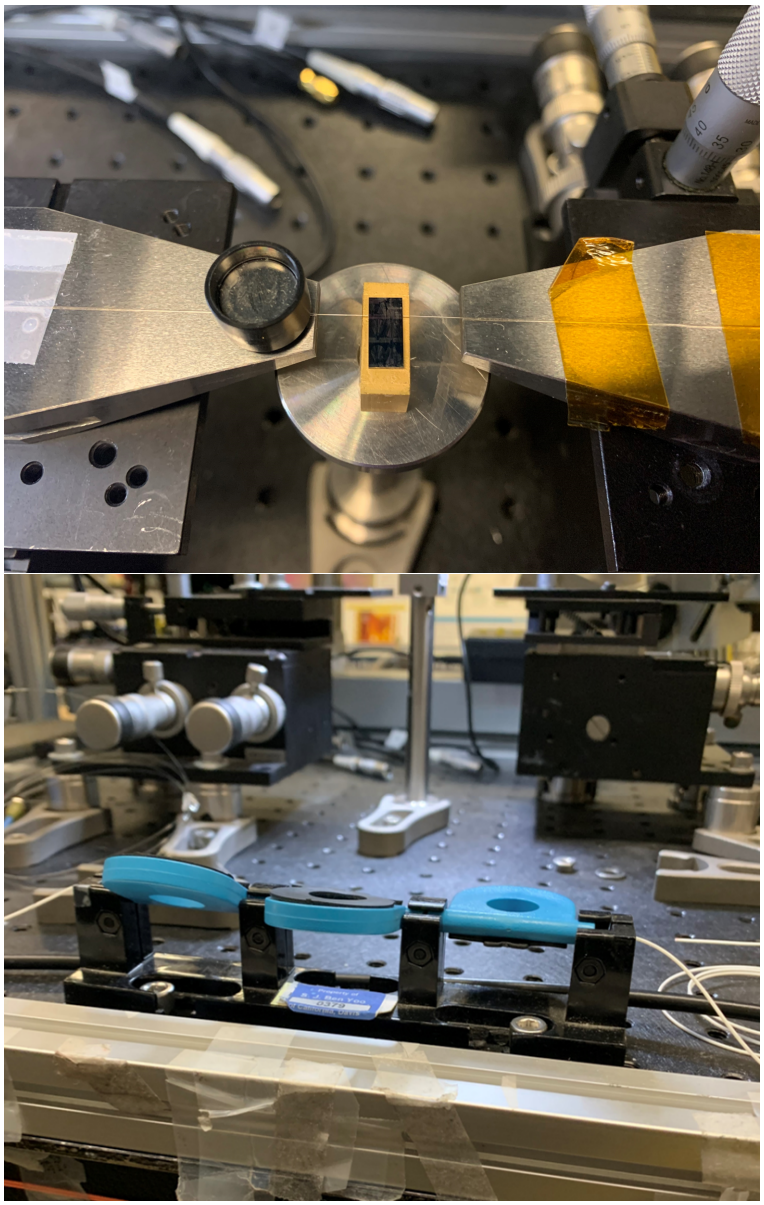

Figure 4.5. Measurement setup and polarization controller.

## 4.3 Reflective AWG measurements

The measurement apparatus of the reflective AWG includes an ASE light source, PC and OSA. The layouts of a regular AWG, center-output RAWG and off-center-output RAWG as well as their measured spectra are shown in the Figure 4.9. The three AWGs are fabricated by myself in the UC Berkeley Nanolab using the 150 nm single-layer SiN platform. Figure 4.9.(a) is a regular 16x16 AWG with 160 GHz channel spacing. Figure

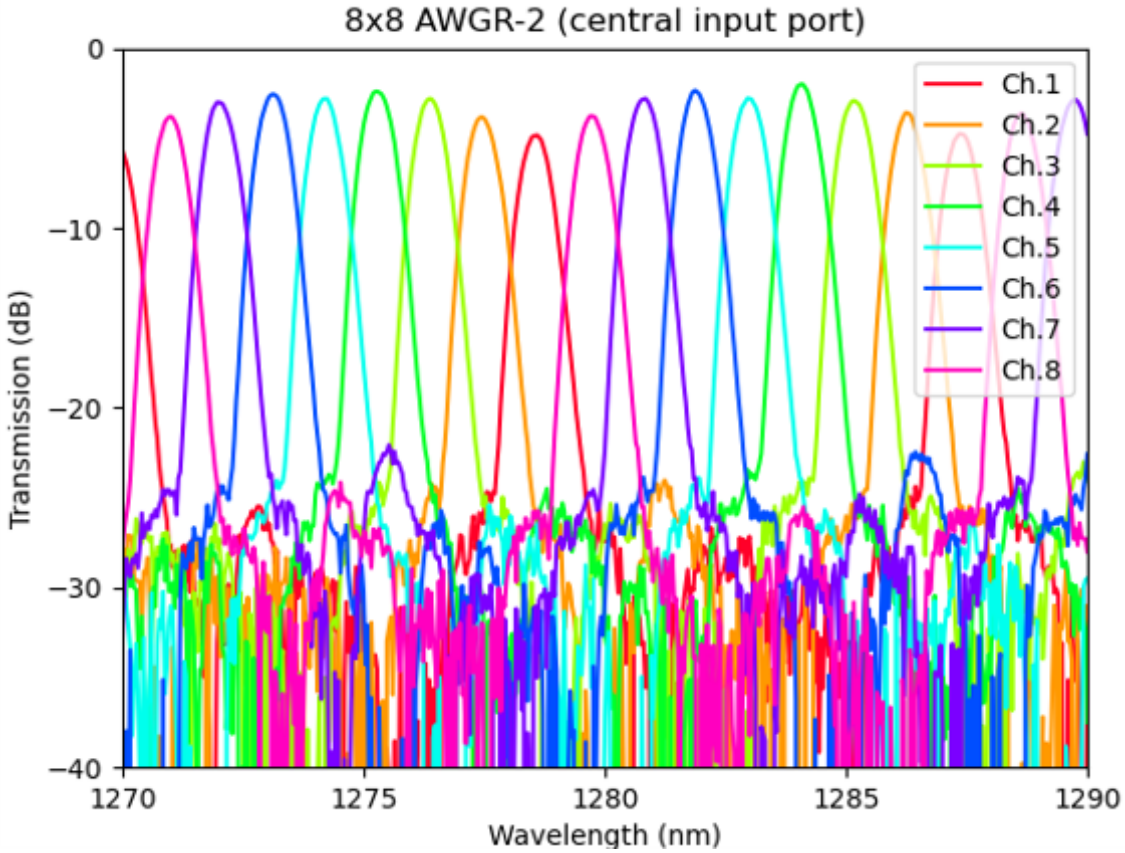


Figure 4.6. Measured spectra of an 8x8 200 GHz channel-spacing circular shape AWGR. The center wavelength is designed to be 1280 nm. The measured center wavelength is 1282.96 nm (0.004% offset). Insertion loss is 2.36 dB; channel spacing is 201.62 GHz (0.81% offset); crosstalk is -20 dB; 3dB passband is 0.66 nm; 3 dB passband channel spacing ratio is 59.90%.

4.9.(c) is a center-output 16x1 RAWG. Figure 4.9.(e) is an off-center-output 15x1 RAWG. Figure 4.9.(e) is basically a half of the AWG (a) with one of the input waveguides using as output waveguides. That is why spectrum Figure 4.9.(f) has an 8-channel offset compared with spectrum Figure 4.9.(b). RAWG Figure 4.9.(c) is specially designed to have the same center wavelength as RAWG Figure 4.9.(e). That is why the other 16 input waveguides are so away from the center.

The size of AWG (a) is 3 mm x 1.8 mm. The size of RAWG (c) and (e) is around 3 mm x 0.7 mm. The size of AWGs can be reduced by half using the reflective-type design which is a huge improvement to achieve a very compact device.

Comparing Figure 4.9.(b) and (f), we can obviously see that the off-center-output

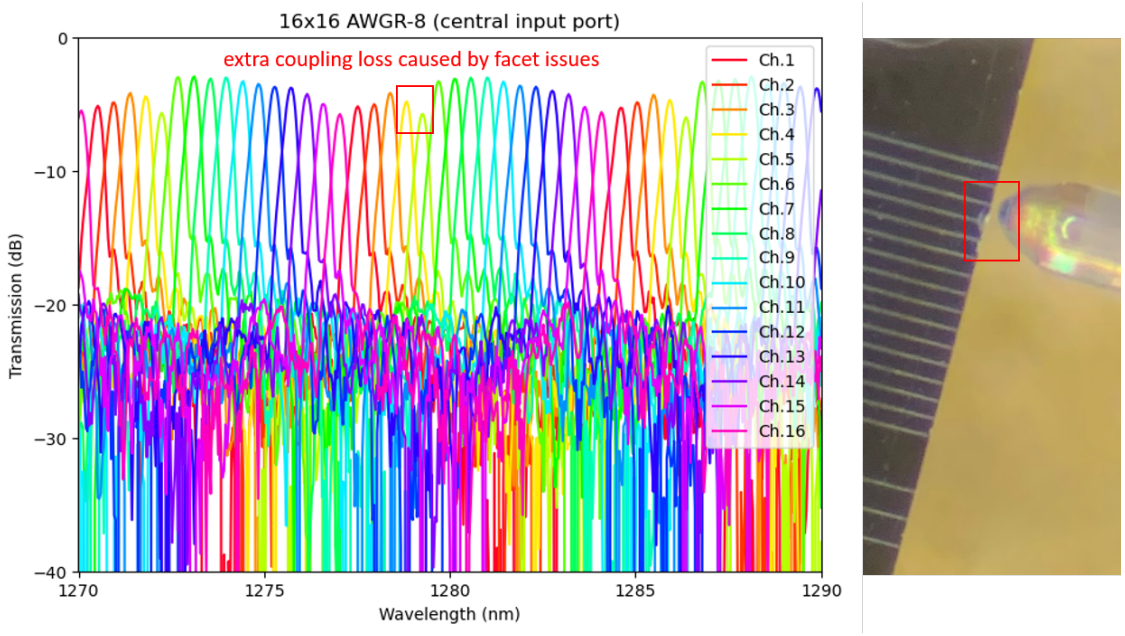


Figure 4.7. Measured spectra of a 16x16 80 GHz channel-spacing box-shaped AWGR. The center wavelength is designed to be 1280 nm. The measured center wavelength is 1280.55 nm (0.04% offset). Insertion loss is 2.98 dB; channel spacing is 80.97 GHz (1.21% offset); crosstalk is -12 dB; 3dB passband is 0.34 nm; 3 dB passband channel spacing ratio is 62.21%. Two channels have extra coupling loss coming from the facet issue.

RAWG introduces an extra insertion loss which is around 5 dB. The loss consists of the star coupler loss and the DBR loss. The relatively large star coupler loss comes from the very-off-centered output waveguides. The DBR high-reflective wavelength window covers the range from 1260 nm to 1290 nm. Comparing (d) and (f), we can see that the farther the input waveguide is from the center, the insertion loss is higher. For example, channel 16 is the farthest input waveguide whose insertion loss is around 27 dB (unusable). Channel 1 is the closest input waveguide to the center, so that it has the lowest insertion loss but not low enough to beat the off-center-output RAWG. In conclusion, there is a trade-off between the device size and the insertion loss.

## 4.4 Thermal-optic tunable AWG fabrication

The center wavelength is highly related to the refractive index of arrayed waveguides and we know the refractive index of SiN and SiO2 is temperature-dependent. As a result, if we can control the temperature of arrayed waveguides, we can tune the center wavelength

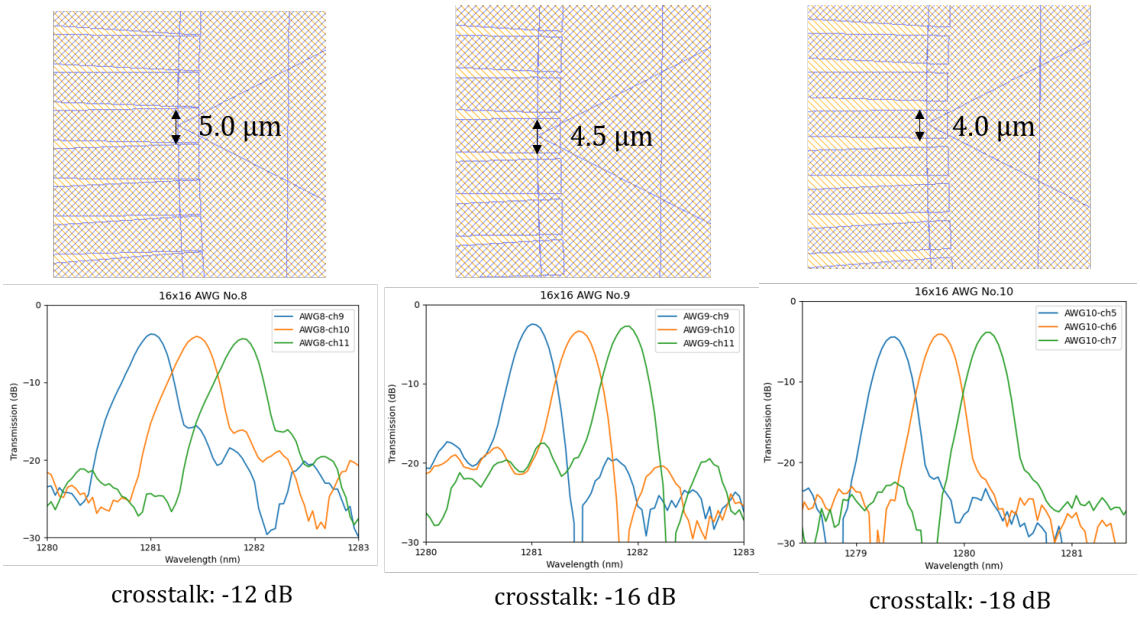


Figure 4.8. Comparison of different input/output port width. The port width controls the passband width. The wider the port is, the wider the passband is.

of the AWG easily. One way to heat AWGs is to place metal heaters on the top of AWGs [22].

Metal heaters are widely used in the thermal-optic tuning device thanks to the reliability and fabrication convenience. The process flow of thermal-optic tunable AWG using two layers of metals is shown in Figure 4.10. All the processes are completed by myself with help from Yichi Zhang. (a) Fabrication starts with a 6-inch oxidation wafer. The SiO2 thickness is 6 $\mu m$. (b) The wafer is deposited with 150 nm SiN using LPCVD. (c) The wafer is deposited with 80 nm amorphous Si using LPCVD. (d) Then the wafer is coated with 0.87 $\mu m$ photoresist. (e) P mark (or alignment mark) is patterned on the photoresist layer using the ASML DUV stepper and the picotrack developer. Because we have three patterned layers on the same wafer, P mark is necessary for the stepper to do the alignment. (f) Using the photoresist layer as the mask, a-Si and SiN layers are etched using ICP etching systems. (g)The remaining photoresist is stripped by the matrix asher. (h) The wafer is coated with BARC and 0.43 um photoresist and then patterned (the waveguide and AWG layer) in the ASML DUV stepper and picotrack developer. (i) The BARC layer is etched in the ICP sts-oxide etching system. (j) a-Si layer is etched in the

ICP sts2 etching system. (k) Photoresist and BARC layers are stripped in the matrix asher. The remaining amorphous Si layer works as the hard mask. (l) Using the amorphous Si layer as the hard mask, the SiN layer is etched using the ICP sts-oxide etching system. (m) The remaining amorphous Si layer is oxidized as a SiO2 layer. (n) The wafer is deposited with 4.15 $\mu m$ SiO2 using LPCVD. (o) To flatten the surface of the wafer, it needs chemical mechanical polishing (CMP). After the CMP, the SiO2 cladding will be thinner. That is why we need to deposit enough SiO2 as cladding in step (n). (p) The wafer is coated with 1 $\mu m$ lift-off resist (LOR) and 0.87 $\mu m$ photoresist. LOR makes it easier to remove the unwanted metal. (q) The wafer is patterned (the first metal layer) in the ASML DUV stepper and the picotrack developer. This is the first metal layer used as a heater. (r) The wafer is deposited with 20 nm Ti and 480 nm Au using the CHA ebeam evaporator in the UC Davis Center for Nano-MicroManufacturing. The thickness needs to be adjusted according to the metal resistance and the power supply. (s) The wafer is immersed in the remover 1165 for 24 hours. The remover 1165 can resolve LOR resist and the metal on the top of LOR and photoresist will be peeled off. (t) Another coating for the second metal layer. (u) Patterning using the ASML stepper and the picotrack developer. (v) The wafer is deposited with 20 nm Ti and 850 nm Au. This metal layer is working as the connection from the heater metal layer to the pad. The connection layer is usually thicker than the heater layer. (w) The wafer is immersed in the remover 1165 for 48 hours to peel off the unwanted metal.

## 4.5 Conclusion

In this chapter, we discuss the fabrication process of single-layer SiN waveguide platform and the fabrication process of thermal-optic tunable AWG. The difference between the single layer SiN waveguide platform fabrication and the thermal-optic tunable AWG fabrication is whether metal heaters are needed. The waveguide layer fabrication parts are actually the same. The measurement results of 8x8 200 GHz channel spacing AWGR and 16x16 80 GHz channel spacing AWGRs show a perfect consistency with the design and simulation, which certificate the feasibility of my AWG design, simulation and fabrica-

tion flow. Also, we successfully demonstrated the first reflective AWG with DBR on SiN platform (to our knowledge).

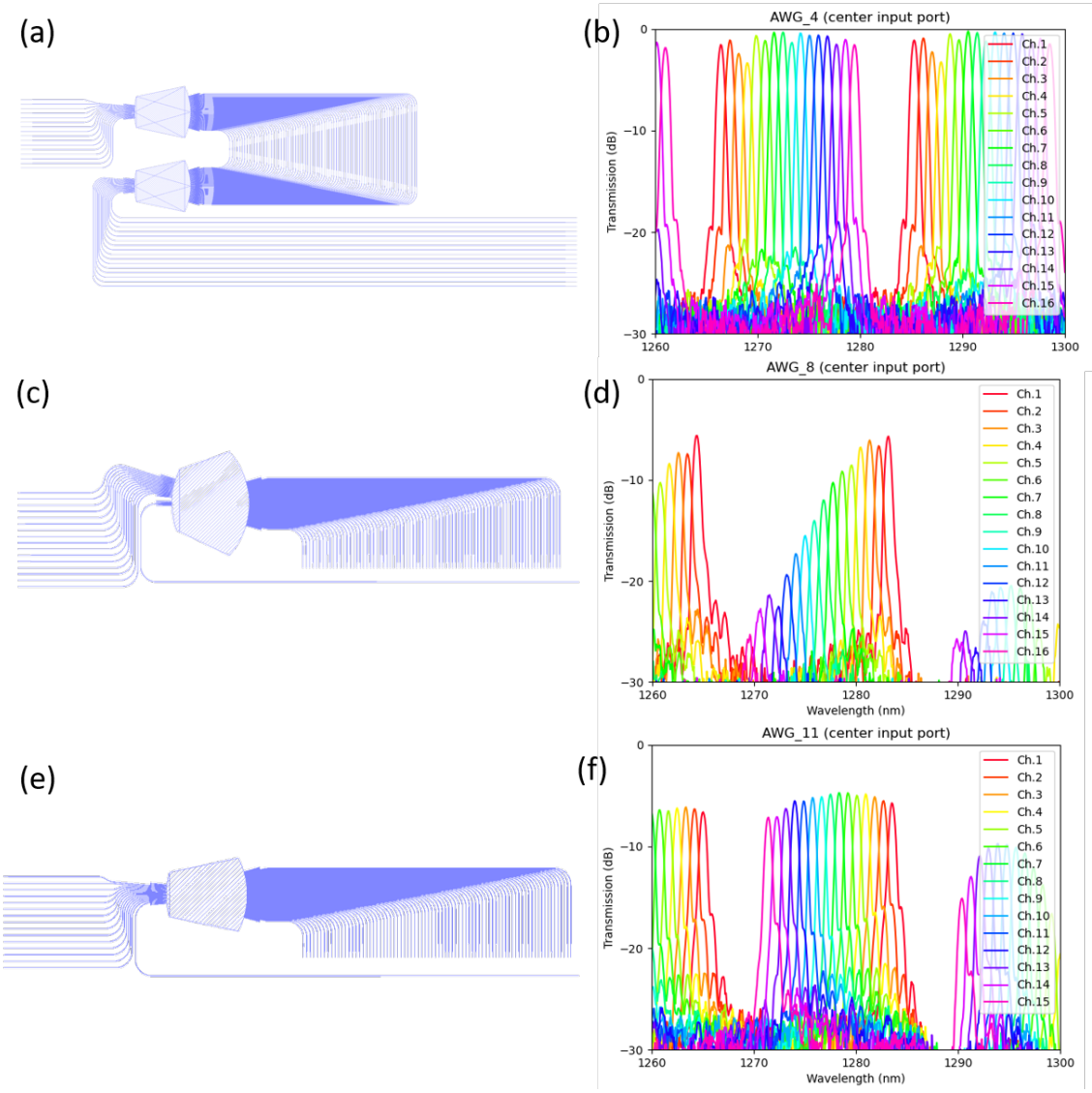


Figure 4.9. Comparison of different RAWG. The three AWGs are fabricated using a 150 nm single-layer SiN waveguide platform. (a) is the layout of the a regular 16x1 160 GHz channel spacing AWG. (b) shows the measured spectrum of (a). The center wavelength is 1273.36 nm; insertion loss is 0.34 dB (calibrated to the straight waveguide); Adjacent crosstalk is -21 dB; Non-adjacent crosstalk is -23 dB; (c) is the layout of a 16x1 160 GHz channel spacing RAWG. The input waveguide comes in the center of starcoupler. To equalize the center wavelength with the other RAWG, the rest output waveguides have to be off-center a lot. (d) shows the measured spectrum of (c). The center wavelength is 1276.8 nm; the minimum insertion loss is 5.70 dB; the channel spacing is 159.58 GHz; the adjacent crosstalk between channel 1 and channel 2 is -15 dB; the non-adjacent crosstalk in channel 1 is -19 dB. (e) is the layout of a 15x1 160 GHz channel spacing RAWG. It is modified from (a) by changing an input waveguide into an output waveguide. (f) shows the spectrum of (e). The center wavelength is 1277.52 nm; the channel spacing is 160.10 GHz; the insertion loss of channel 1 is 4.7 dB; the adjacent crosstalk between channel 1 and channel 2 is -14 dB; the non-adjacent crosstalk of channel 1 is -19 dB.

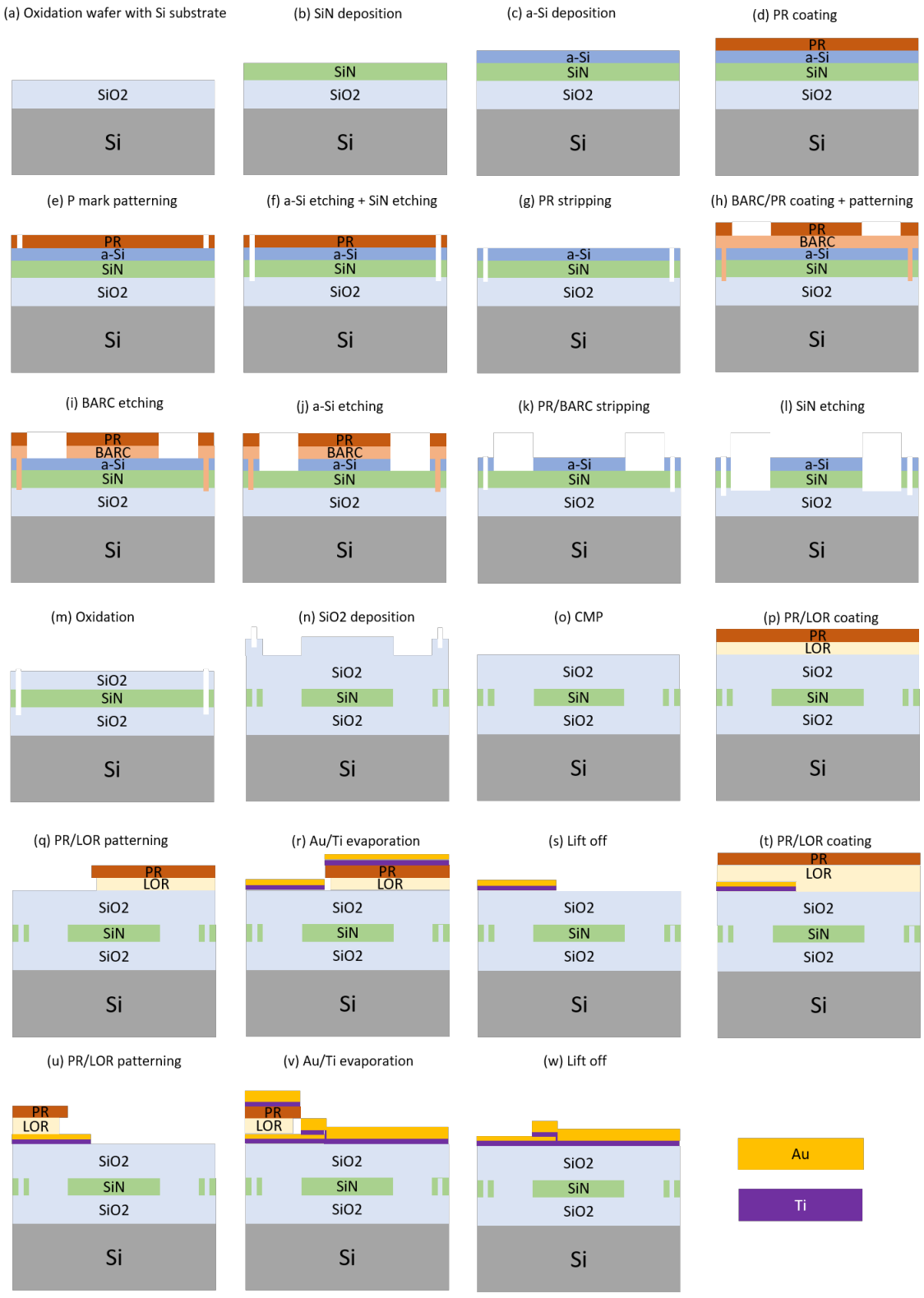


Figure 4.10. Thermal tunable AWG fabrication process flow.

# Chapter 5

# Applications

## 5.1 Optical arbitrary waveform generator (OAWG) with ring assisted Mach-Zehnder interferometers (RAMZI)

OAWG is a flexible bandwidth communication system that can generate continuous and high fidelity arbitrary waveform by cutting a spectrum into smaller spectral slices and modulating them in the time domain and combining them to create the targe spectrum [13].

The basic idea of dynamic OAWG is shown in Figure 5.1. The input signals are frequency combs. Each comb line is designed to be inside one narrow passband channel of the demultiplexer. The comb lines are demultiplexed into separate spatial waveguides. On each waveguide, there is a high-speed I/Q modulator controlled by the software. The I/Q modulator will create a slice of the target spectrum based on a DSP program. Next, these spectrum slices will be multiplexed to the same waveguide by a broadband multiplexer. The combined spectrum is the generated spectrum.

The OAWG consists of three components – demultiplexer, I/Q modulator, and multiplexer. Demultiplexer can be a narrow passband AWG demultiplexer as shown in Figure 5.2. The broad passband multiplexer can be a flat-top broad passband AWG multiplexer as shown in Figure 5.3. Theoretically, the demultiplexer and the multiplexer should work on the same wavelengths channels. However, AWG center wavelength is highly

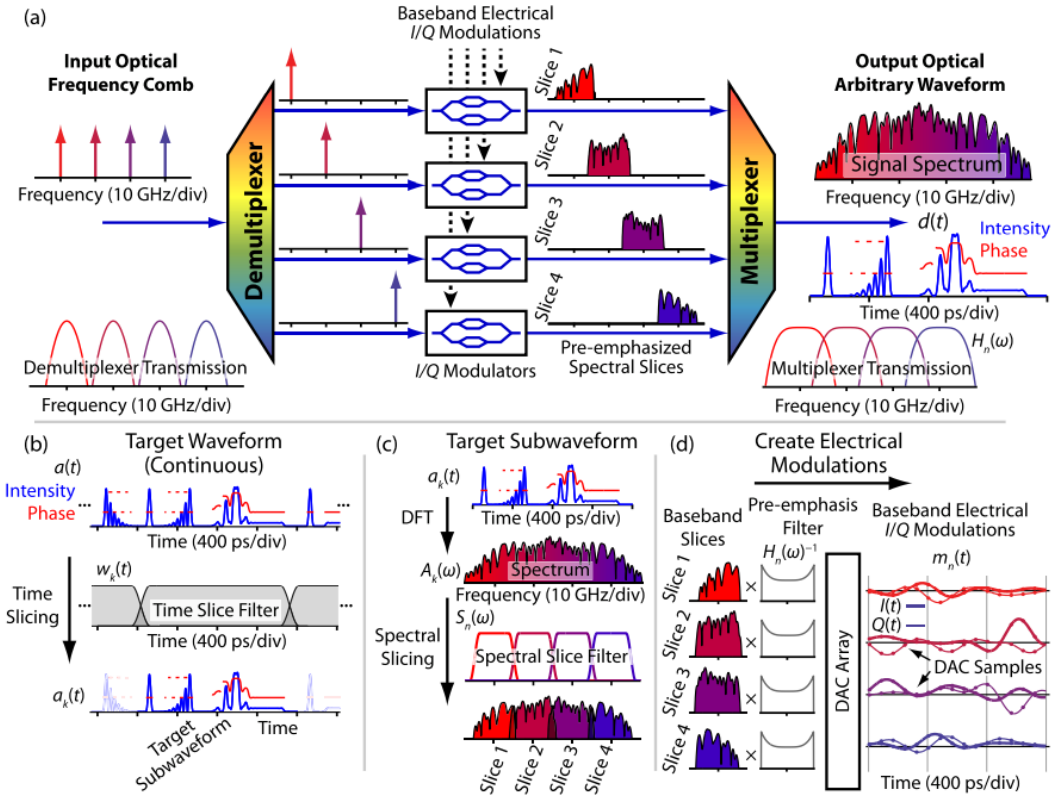


Figure 5.1. The picture is from [13]. (a) Each line of an OFC is simultaneously and independently modulated to create the desired slices. (b) In DSP, the target waveform is temporally sliced into subwaveforms. (c) The subwaveforms are spectrally sliced. (d) Baseband electrical I/Q modulations are calculated and produced.

fabrication-sensitive. Even two same AWGs on the same die can have different center wavelengths. Because the working wavelengths of the demultiplexer and the multiplexer should be aligned accurately, we can add heaters to control the center wavelength for both of them or we can replace the multiplexer with a $N \times 1$ tree. The last component is the I/Q modulator which provides four-quadrature modulation based on Equation 5.1.

$$\frac{E_{out}(t)}{E_{in}(t)} = \frac{1}{2}cos(\frac{u_I(t)\pi}{2V_\pi}) + j\frac{1}{2}cos(\frac{u_Q(t)\pi}{2V_\pi}) \tag{5.1}$$

An I/Q modulator consists of two Mach-Zehnder modulators (MZI). Compared with traditional electro-optic MZI, Ring-assisted MZI (RAMZI) provides low drive voltage and large extinction ratio [23]. The basic idea is to use the push-pull operation on two arrayed ring modulators. As shown in Figure 5.4, when the working wavelengths of both rings are

exactly at the laser wavelength, the transmittance of each ring is at the lowest value. If the $\pi$ phase shift from the thermal phase shifter (shown in Figure 5.5 (c)) is considered, the total transimittance will be lower. When the working wavelengths of the two rings are pushed to the opposite directions. At the laser wavelength, the transmittance of each ring resonator is relatively high. Because of the $\pi$ phase shift caused by the over coupling condition and the $\pi$ phase shift caused by the thermal phase shifter, the total transmittance will be even higher (theoretically to be 1).

The OAWG with RAMZI is shown in Figure 5.5 (d), the extinction ratio of the RAMZI is about 40 dB when the push-pull voltage difference is 3.5 V based on the simulation result. I did the design part and these devices are being fabricated by AIM Photonics. Figure 5.6 shows the complete layout of the OAWG with AWG, RAMZI and high speed signal metal routing lines.

## 5.2 Optical synaptic interconnection system

Recently, there have been a lot of attempts to implement neuromorphic computation on integrated chips. For example, Intel labs have fabricated a spiking neural networks modeling chip with programmable synaptic learning ruls on it [24]. Even if it is an extremely sophisticated system, the basic function is still integrating the inputs from other neurons with different weights and generating spike responses. These weights need to be stored and updated arbitrarily according to the outputs and feedback of the neural network. In other words, it is like an "arbitrary weighted addition". This function is implemented by one significant component of a neural network named synaptic interconnection.

The modern optical synaptic interconnection should be built on a wavelength-dimension multiplexing (WDM) coherent system. In that case, both intensity, wavelength, and phase information can be treated as individual labels to recognize a symbol. In our WDM system, arrayed waveguide grating (AWG) works as the demultiplexer to route signals to their destinations based on their wavelength. All devices used in my configurations are designed for TE polarization.

In this section, two main possible architectures for the implementation of an optical

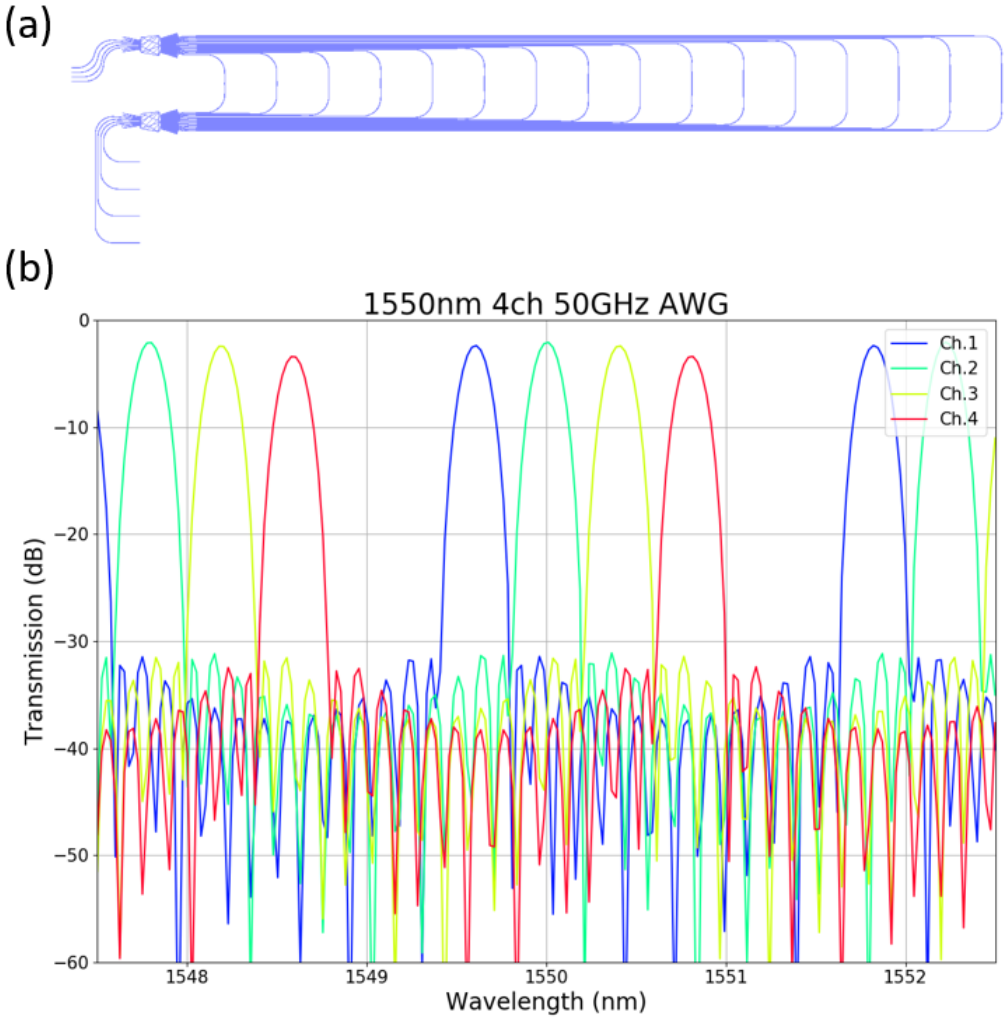


Figure 5.2. One design of a $Si_3N_4$ narrow passband AWG demultiplexer. The demultiplexer has 4 inputs and 4 outputs, but only the center input will be used. The center wavelength is designed to be 1550 nm; channel spacing is 50 GHz. The thickness of the $Si_3N_4$ layer is 220 nm. (a) The layout of a narrow passband AWG demultiplexer (b) The simulated spectrum of the narrow passband AWG demultiplexer.

synaptic interconnection system are discussed. as well as corresponding methodologies to achieve the "arbitrary weighted addition" function.

The first architecture of the optical synaptic interconnection is based on the "spatial-separated modulation" method. The basic idea is to demultiplex signals with different wavelengths spatially and then modulate them individually and multiplex them together. Previous works have used a similar method to implement an optical arbitrary waveform generation (OAWG) transmitter [25]. Figure 5.7 shows a simplified 4-channels configura-

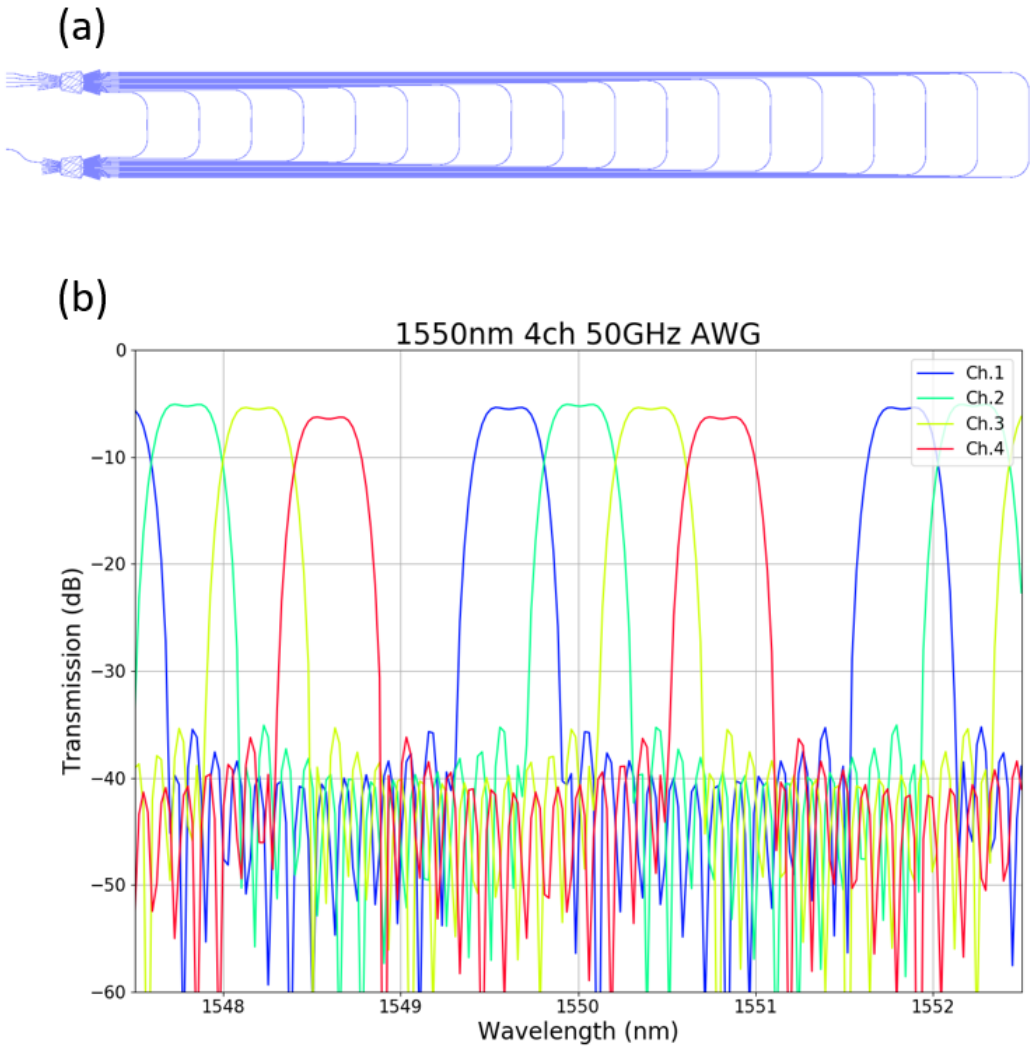


Figure 5.3. One design of a $Si_3N_4$ flat-top broad passband AWG multiplexer. The multiplexer has 4 inputs and 1 output. The center wavelength is designed to be 1550 nm; channel spacing is 50 GHz. The thickness of the $Si_3N_4$ layer is 220 nm. (a) The layout of a flat-top broad passband AWG multiplexer (b) The simulated spectrum of the flat-top broad passband AWG multiplexer.

tion using the "spatial-separated modulation" method. The laser box shown in the figure is a complex system to generate 4 narrow optical pulses $x_1$,$x_2$,$x_3$,$x_4$ with 4 different wavelengths ($\lambda_1$,$\lambda_2$,$\lambda_3$,$\lambda_4$) and import them into the demultiplexer at the same time. Assuming signal $x_i$ goes the $i-th$ output of the demultiplexer, the signal is modulated by the intensity modulator and phase modulator. Intensity modulators and phase modulators are controlled by digital signal processing (DSP) algorithms through a computer. Signal $x_i$ is

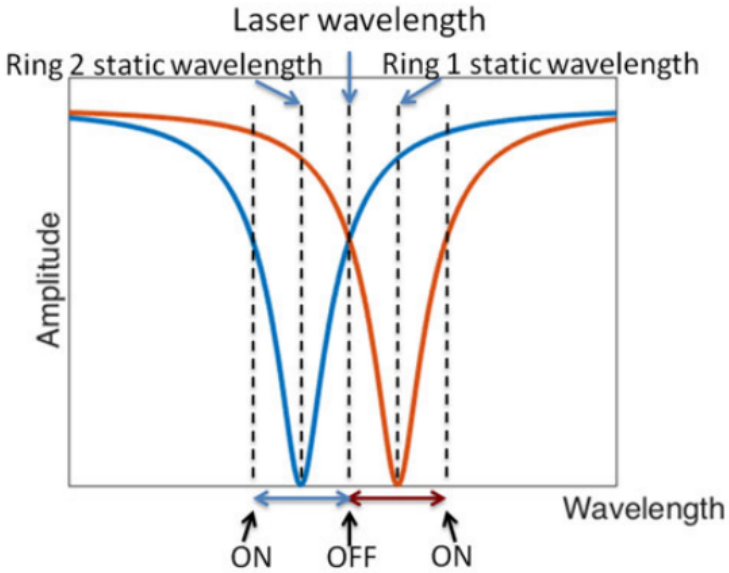


Figure 5.4. Ring-assisted MZI working principle [23].

multiplied by weight $w_i$ after modulated by the intensity modulator. The signal received by the photodiode is $w_1\ x_1 + w_2\ x_2 + w_3\ x_3 + w_4 x_4$. In the form of matrix calculus, it can be written as:

$$y = \mathbf{w^T x} \tag{5.2}$$

$\mathbf{w}$ and $\mathbf{x}$ are $N \times 1$ vectors. However, in the synaptic interconnection, we want to obtain multiple returns rather than only one return. In the form of matrix calculus, we want to solve the matrix multiplication:

$$\mathbf{y} = \mathbf{w^T x} \tag{5.3}$$

In Equation 5.3, $\mathbf{y}$ is a $M \times 1$ vector; $\mathbf{w}$ is a $N \times M$ matrix; $\mathbf{x}$ is a $N \times 1$ vector. Fortunately, it is still doable using the same configuration shown in Figure 5.8. The key point is to utilize time-dimension multiplexing (TDM). At time slot 1, four signals $x_1$,$x_2$,$x_3$,$x_4$ are imported into the demultiplexer and the photodiode receives response $y_1$. At time slot 2, the same four signals $x_1$,$x_2$,$x_3$,$x_4$ are imported into the demultiplexer. For this time, weights are changed via intensity modulators. Then the photodiode receives

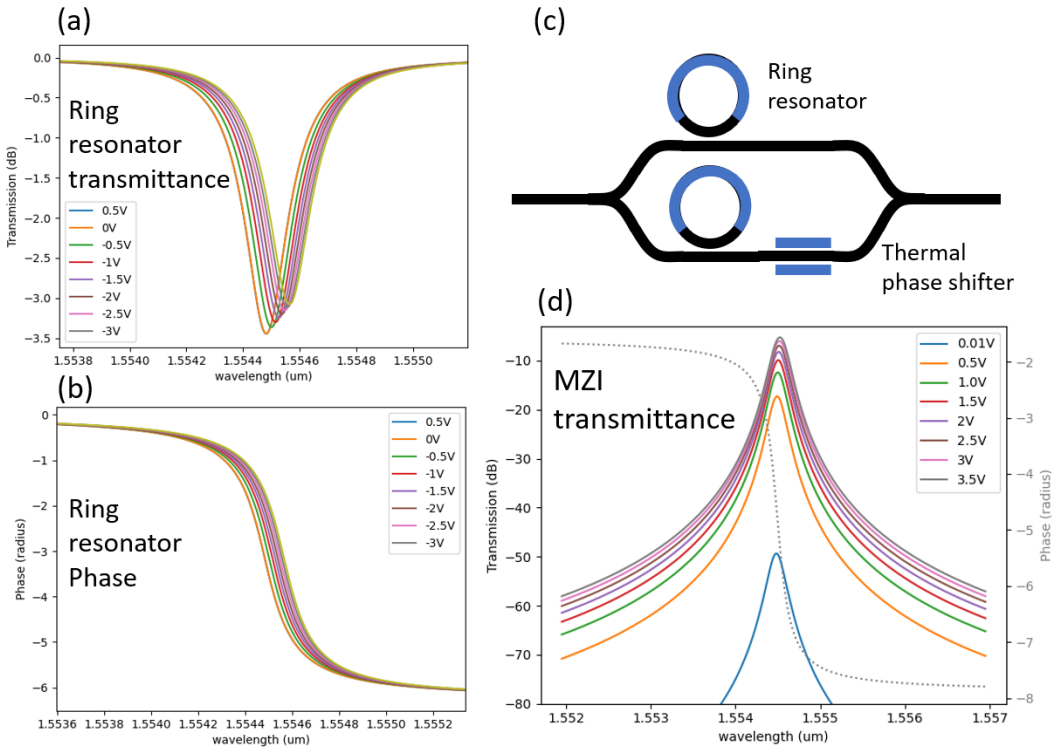


Figure 5.5. (a) The ring resonator transmittance. (b) The output field phase of the ring resonator vs wavelength. (c) The schematic view of a RAMZI. (d) The transmittance of the MZI. The distinction ratio can achieve higher than 50 dB (voltage difference changing from 0.01 V to 3.5 V).

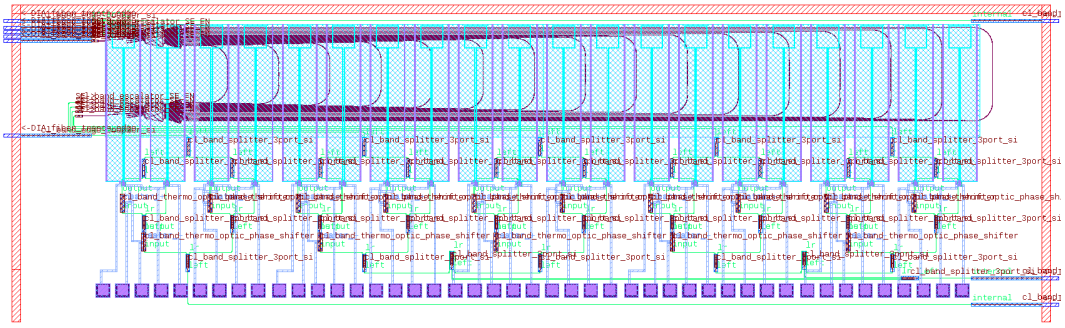

Figure 5.6. OAWG layout.

response $y_2$. The speed of this system is bounded by the speed of computer-controlled modulators.

Another configuration to implement the matrix multiplication instantaneously is shown in Figure 5.8. The idea is manipulating multiple signals on one certain connection between the demultiplexer and the multiplexer at the same time. To meet this requirement,

there are two problems to solve. The first problem is how to multiplex multiple signals on one waveguide without signal mixing. The second problem is how to manipulate these signals on the same waveguide individually.

To solve the first problem, an arrayed waveguide grating router (AWGR) is utilized. As shown in Figure 3.1, AWGR is an all-to-all interconnection router, which routes signals based on their positions and wavelengths. One of the most important properties of AWGR is that these signals from different input ports but routed to the same output have different wavelengths so that they will not be mixed up.

To solve the second problem that signals with different wavelengths need to be manipulated individually, the continuously tunable, wavelength-selective optical buffers are used. Optical buffers can apply variable delays to wavelengths of choice [26]. The delayed pattern is shown in Figure 5.9. The delay is applied to the signal with wavelength $\lambda_1$ whereas it does not affect the signal with wavelength $\lambda_2$ appreciably. Apart from applying phase delay, intensity attenuators can be added on these rings to make them wavelength-selective. One challenge is that the free spectra range (FSR) and center wavelength must match with AWGR perfectly.

The configuration in Figure 5.8 can support $N$ inputs and obtain $N$ outputs at the same time. It converts multiple devices shown in the Figure 5.7 into one device. The demultiplexer and multiplexer shown in the Figure 5.8 are both $N \times N$ AWGRs. Signals are identified based on two attributes — the wavelength and the input port position. As a result, operation on each signal is done individually. Also, almost all the components used in the configuration in Figure 5.8 have been demonstrated successfully ([26]) which gives us sufficient confidence to give it a try. The disadvantage is that it is not easy to align wavelengths for two AWGRs and $N^2$ optical buffers. To solve this problem, we can use the thermal tuning method from [22].

To reduce the complexity of the synaptic interconnection, we propose another architecture using only one AWGR. The configuration is shown in Figure 5.10. The basic idea is to manipulate signals on arrayed arms. The most significant property is that only phase modulators are used on the optical buffers, which means that the system can be

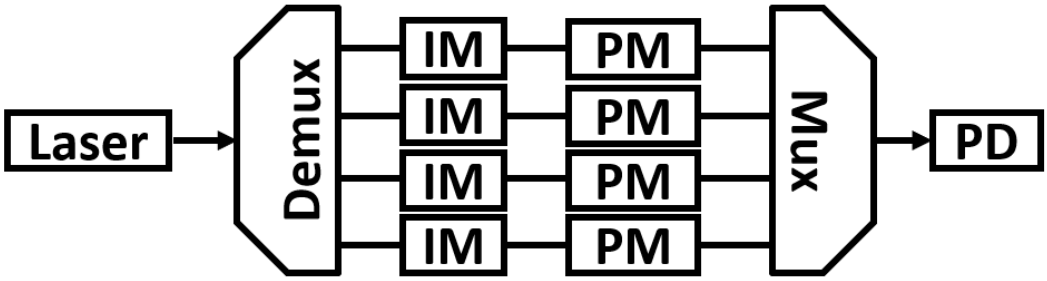


Figure 5.7. Optical synaptic interconnection system: spatial-separated modulation. Demux: demultiplexer; IM: intensity modulator; PM: phase modulator; Mux: multiplexer; PD: photodiode.

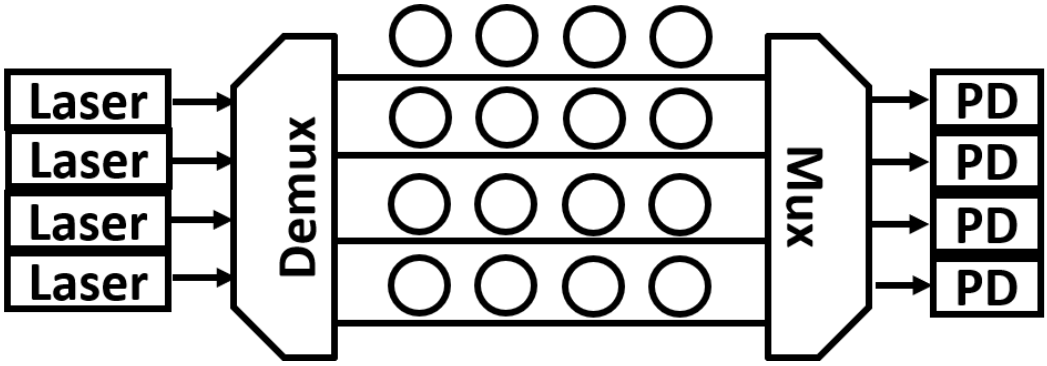


Figure 5.8. Optical synaptic interconnection system: spatial-separated modulation. This configuration has multiple inputs and multiple outputs. Demultiplexer and multiplexer are AWGRs. Rings are continuously tunable, wavelength-selective optical buffers. On each connection, there are N (number of channels) optical buffers designed for the N channel wavelengths.

lossless theoretically. If a signal $x_i$ with wavelength $\lambda_i$ is transmitted into the AWGR, it will be diffracted and propagating in the free propagation region (FPR), and be coupled into multiple arrayed arms. On each arm, the electric field is manipulated by a phase modulator designed at wavelength $\lambda_i$. At the output of the arrayed arms, these fields accumulate, get diffracted once again in the second FPR and then get coupled into output waveguides. The energy obtained by each output port can be tuned arbitrarily by these phase modulators. If all the N signals (with N different wavelengths) are considered, then it works like an arbitrary weighted addition.

Even though this single AWGR synaptic interconnection is simpler in terms of configuration, it is much more complex in manipulating these phase shifters because the original signal is truncated into several slots spatially by these arrayed arms. We need to make

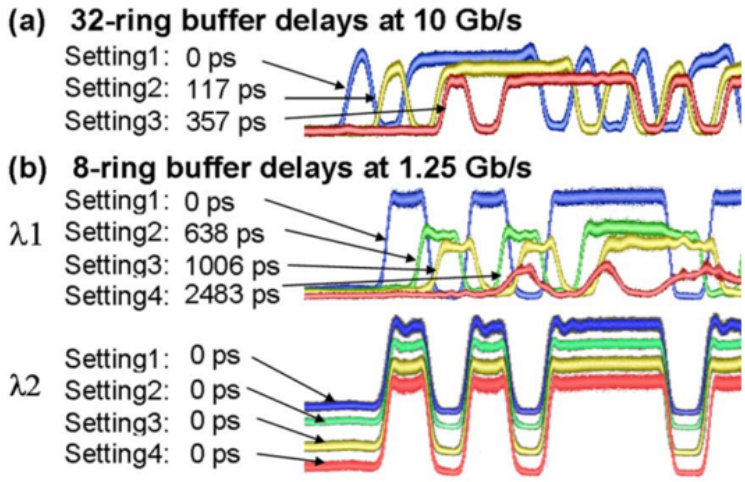


Figure 5.9. (a) The signal when 32-ring buffer delays at 10 Gb/s. (b) The signal when 8-ring buffer delays at 1.25 Gb/s [26].

sure the shape of the diffracted field at the output waveguides are what we want. In fact, it is extremely hard because for one wavelength we have M (number of arrayed arms) phase modulators to tune individually. A small change in one phase modulator will affect the energy distribution at output ports a lot.

All in all, I came up with two architectures of synaptic interconnection systems and I have tried particle swarm optimization (PSO) algorithm to train the phase arrayed. I also came up with an iterative algorithm to divide all the arrayed waveguides into several groups to train them individually. My colleagues can do more advanced investigations based on my programs.

## 5.3 WDM laser (passive part)

We design a WDM laser that includes a 32 channel RSOA array, and two interleaved 16-channel SiN AWG multiplexers with 160 GHz spacing and 80% reflectivity at O-band (see Figure 5.11). We are using the 150 nm thickness SiN platform for our fabrication with the optimized waveguide width and angle to match the far-field mode from the Freedom Photonics laser source. The two interleaved 16-channel AWGs have 16 angled input ports and one output port connected with the SGDBR. The wavelength difference of the two AWGs is equal to half channel spacing (80 GHz). Two long vertical waveguides with the SGDBR are connected by an optical interleaver. To align the channel wavelengths of

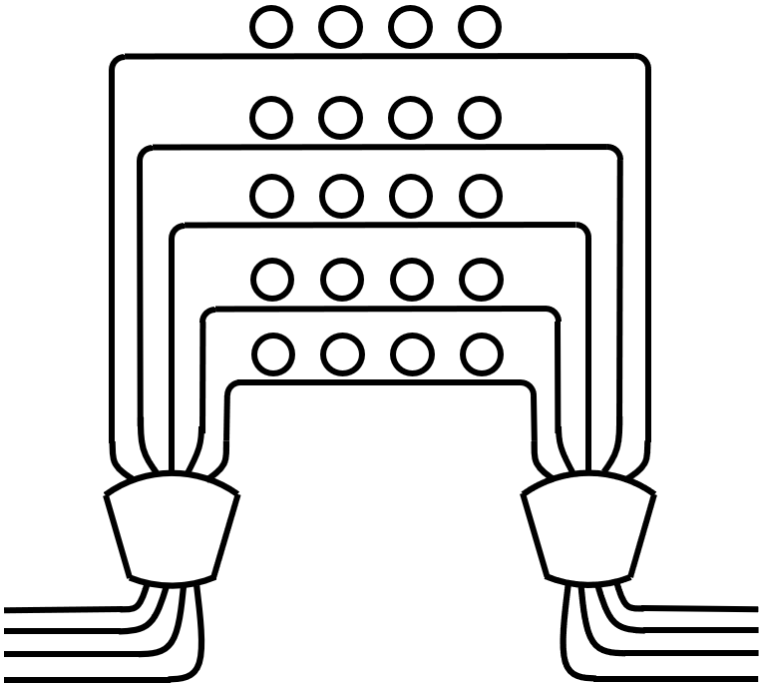

Figure 5.10. Optical synaptic interconnection system: single AWG synaptic interconnection. The synaptic interconnection consists of an AWGR and variable wavelength-selective optical buffers on each arm. Only phase modulators are used on the optical buffers.

the AWG and the SGDBR, thermal-optic tuning is utilized, which means the fabrication process flow mentioned in the previous chapter needs to be used. All the fabrication processes are done by myself with help from Yichi Zhang in the UC Berkeley Nanolab and the UC Davis Center for Nano-MicroManufacturing. The complete layout of WDM laser is shown in Figure 5.17 (a). Although the design of Figure 5.17 was intended, due to the error, the waveguides interfaces with RSOAs were incorrectly placed in a mirror image. The blue line layer is the waveguide layer including input/output waveguides, AWGs, interleavers, and SGDBRs. The brown layer is the metal heater layer designed to heat the AWG and the SGDBR. Metal heaters are connected to the multiple pads on the north side of the chip on the metal connection layer whose color is orange in subplot (a). Nine fabricated chips are shown in the subplot (b). All fabrication processes are completed by myself at the UC Berkeley Marvell Nanolab and the UC Davis Center for Nano-MicroManufacturing. The process flow exactly follows the thermal-optic tunable AWG fabrication discussed in the previous chapter.

The simulated spectra of two interleaved 16-channel SiN AWG multiplexers with 160 GHz spacing are shown in Figure 5.12. The simulated center wavelengths of the two AWGs are 1280.05 nm (0.005% offset) and 1280.48 nm (0.003% offset). The channel spacing is 160.29 GHz (0.18% offset). The insertion loss is lower than 2dB and the crosstalk is less than -35 dB. 3 dB passband is 45.66% of the channel spacing which can be adjusted by the input/output port width. From the reference [27] , the transfer function of an interleaver is

$$H^R = \frac{t - p^2\gamma exp(i\theta)}{1 - t\gamma exp(i\theta)}$$

We have $n_{eff} = 1.515606$, $N_g = 1.739152$, $\Delta f = 160$ GHz. Then we can calculate the delay length of two arms is $2\Delta L = 2154.74\,\mu m$ and the ring radius is $r = 342.94\,\mu m$. Based on the equation, the calculated spectra are shown in Figure 5.13.

In the test run masks, various AWGs, reflective AWGs, direction couplers, interleavers are placed. The testing AWGs include AWGs with different port widths and different numbers of arrayed arms. The testing reflective AWGs exhibit different center wavelengths and different I/O port widths. The testing directional couplers include different gap and coupling length designs. The testing interleavers adopt different delay-line designs. The measurement results of the two AWGs on the left and right are shown in the Figure 5.14. The center wavelengths of these two AWGs are designed to have an 80 GHz offset because we want to interleave them using an interleaver. The measurement results of directional couplers and interleavers are shown in the Figure 5.15 and the Figure 5.16. We can see that both the directional coupler and the interleaver achieved the desired performance.

The WDM laser (passive part) measurement setup is shown in the Figure 5.18. The input lens fiber is fixed and the output lens fiber can be moved in the north-south direction to be aligned with respect to these angled waveguide tapers. Figure 5.18 (c) and (d) show how lens fibers are aligned with input and output waveguides. The measured results are shown in the Figure 5.19. We can see that the interleaver is working well with the AWG in the range from 1290 nm to 1300 nm and less than 1265 nm. However, SGDBR seems to be not aligned with any of these channels. The center wavelength of SGBDR needs further testing.

Figure 5.20 shows an updated layout of the passive part of the WDM laser with correct waveguide angles. The previous error of waveguides inferfaces with RSOAs have been corrected from mirror image angles to 180 degree rotated angle to allow RSOAs with angled facets to interface. As a result, RSOAs with the same angled facet interfaces can be used on both sides. The only difference is the one on the East needs to be rotated by 180 degrees. The output waveguides of the new layout are pointed to the south with four more loopback waveguides. This modification makes it easier for Freedom Photonics to align the output fiber array.

Because of the long cavity length caused by the SGDBR and AWG, there are multiple longitudinal modes in one channel spacing of AWG passband. To reduce the cavity length, we can replace the regular AWG with a reflective AWG. The SGDBR can be replaced with a Sagnac mirror and a ring filter, or a ring reflection injection locking filter. The layouts of the four alternative WDM lasers are shown in Figure 5.21.

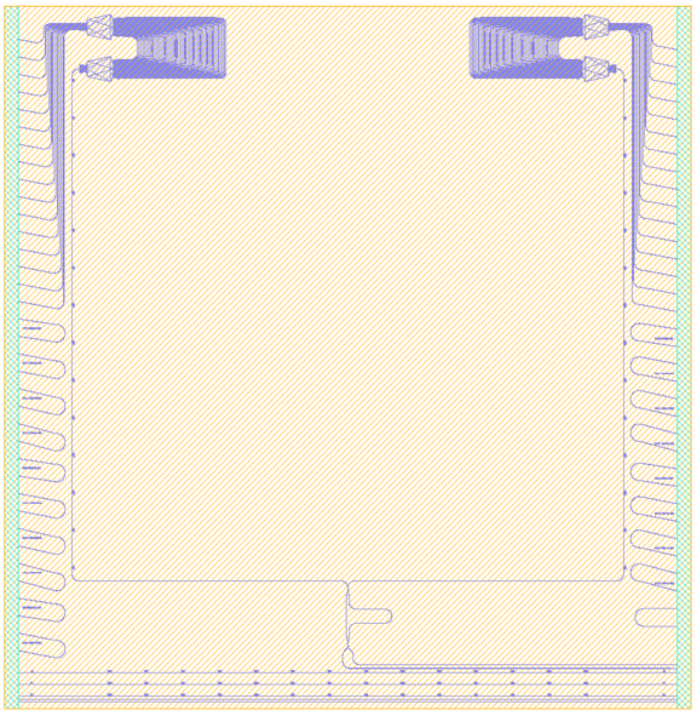

| Item | value |
|---|---|
| Wavelength | 1280 nm |
| Channel spacing | 160 GHz |
| WG thickness | 150 nm |
| SM WG width | 1.2 um |
| MM WG width | 1.9 um |
| Input/output port width | 4.0 um |
| Input/output port spacing | 0.68 um |
| Arrayed arm port width | 3.0 um |
| Arrayed arm spacing | 0.25 um |
| Arrayed arms number | 64 |
| Channel number | 16 |
| Path length difference | 49.92 um |
| Focal length | 397.25 um |
| Grating order | 60 |

Figure 5.11. O-band WDM laser with SGDBR. The design parameters of the AWGs are shown in the table. Even though this design was intended for fabrication, a wrong file with the waveguides oriented in the mirror image has been taped out for mask manufacturing.

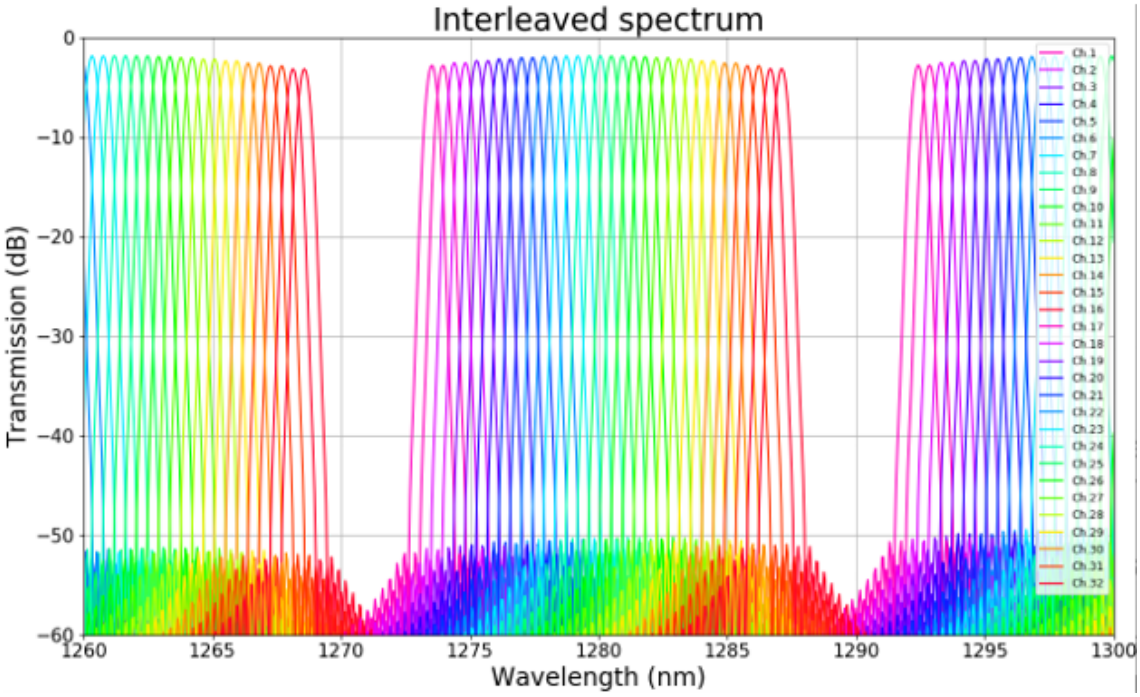


Figure 5.12. The simulated spectra of two interleaved 16-channel SiN AWG multiplexers with 160 GHz channel spacing. The simulation process includes Fraunhofer diffraction calculation, mode coupling calculation, and the eigenmode calculation using Lumerical MODE solution.

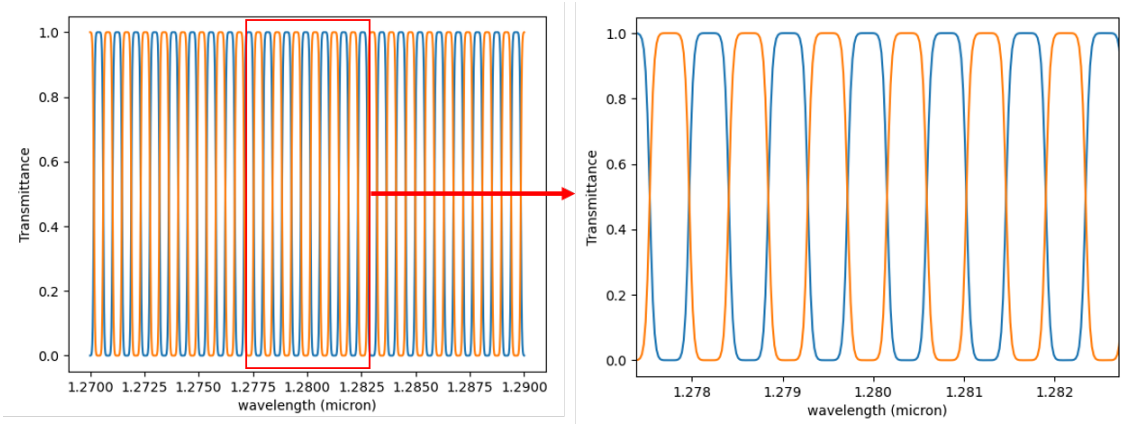


Figure 5.13. The calculated spectra of interleaver. The channel spacing is 79.9 GHz.

## 5.4 Conclusion

In this chapter, three complex system-level applications are introduced. The first one application – OAWG with RAMZI can work to generate arbitrary waveform by spectrum slicing and high-speed modulation. It is being fabricated by AIM Photonics. In the second application – synaptic optical interconnection system, I propose two possible

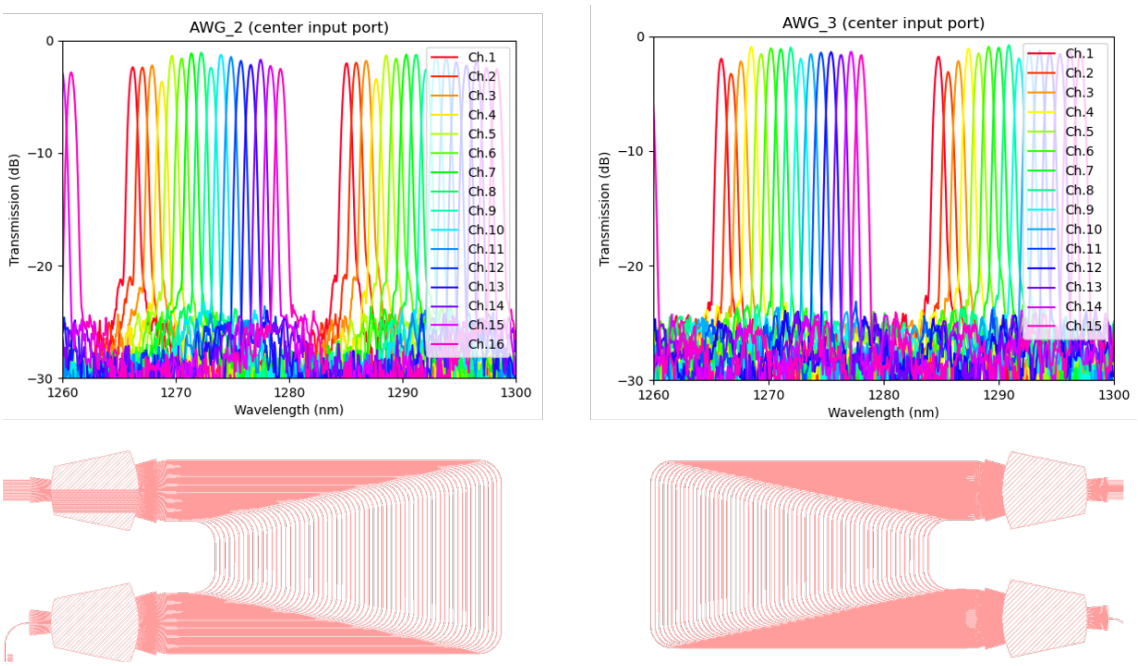


Figure 5.14. The measurement results of the two AWGs. The center wavelength of the left AWG is 1273.12 nm; insertion loss is 1.08 dB; channel spacing is 159.07 GHz; adjacent cross talk is -20 dB. The center wavelength of the right AWG is 1272.78 nm; the insertion loss is 0.98 dB; the channel spacing is 159.02 GHz; the adjacent crosstalk is -19.5 dB.

architectures including "spatially-separated modulation" and "single AWG modulation". The "spatially-separated modulation" is similar to the OAWG architecture and the "single AWG modulation" is original and much more difficult to achieve. In the last application – WDM laser, I fabricate and test some parts including AWGs, directional couplers, interleavers and the WDM laser passive part. AWGs, directional couplers and interleavers are working well. The center wavelength of SGDBR needs to be further tested. Once AWG, interleaver and SGDBR are s aligned, the WDM laser passive part will be completed and waiting to be combined with the gain block from Freedom Photonics.

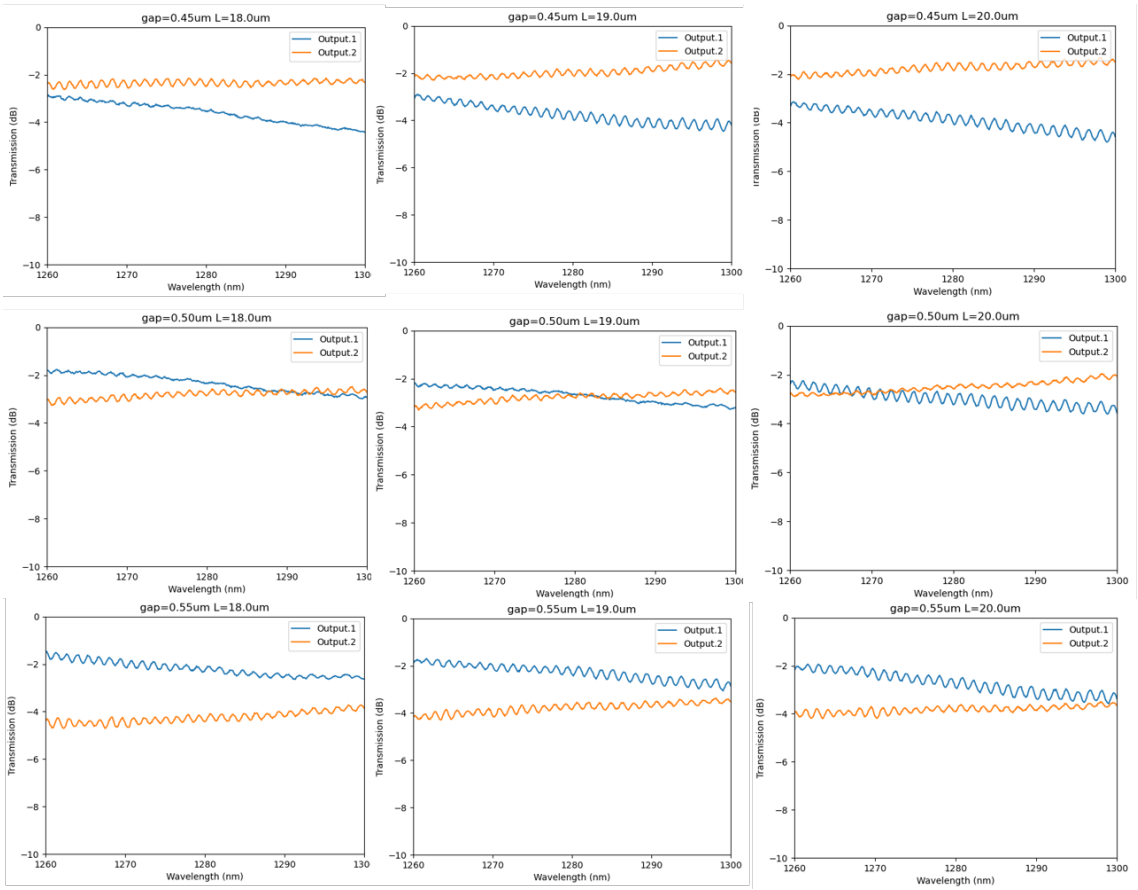


Figure 5.15. The measurement results of 9 different directional couplers (calibrated to straight waveguides). The best 50:50 energy equal distribution happens when the gap is $0.5\mu m$ and the coupling length is $19.0\mu m$.

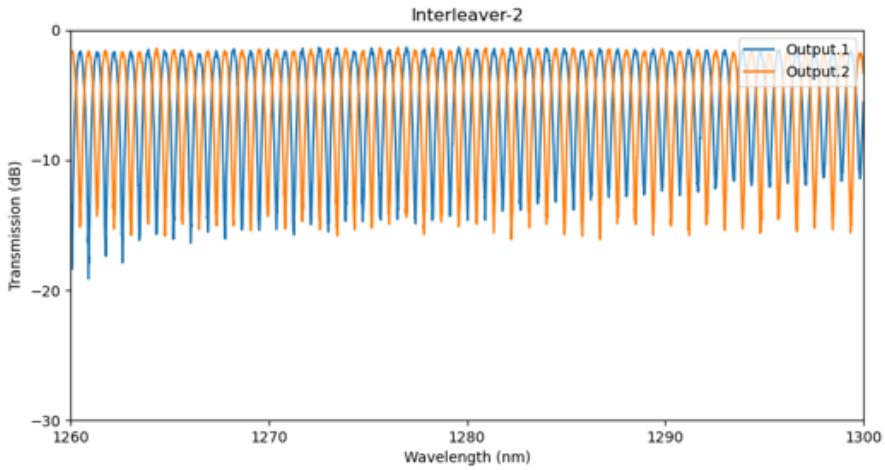


Figure 5.16. The measurement results of an interleaver.

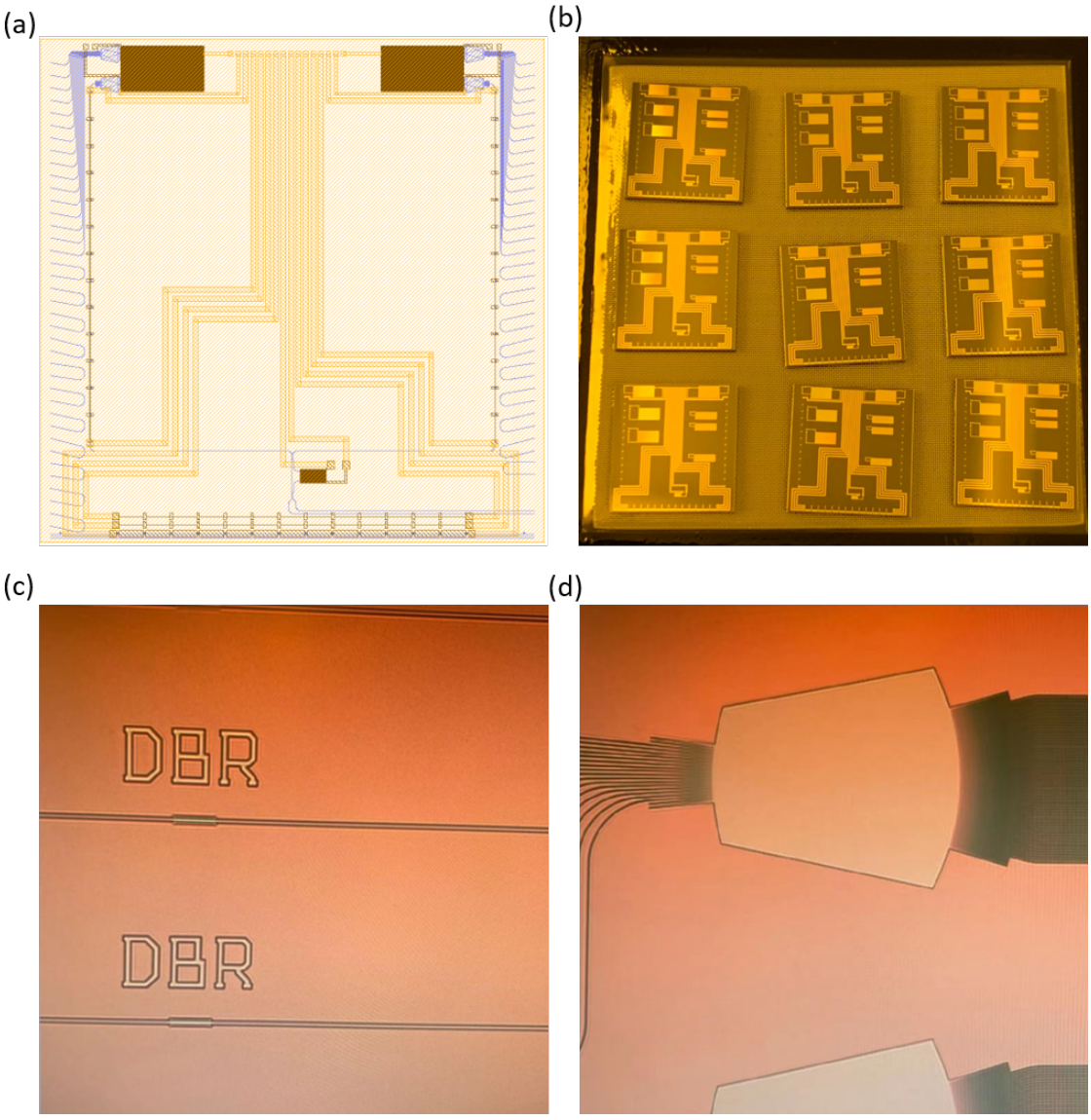


Figure 5.17. (a) The WDM laser layout with metal heater layer and metal connection layer. (b) Photo of 9 fabricated WDM laser chips. (c) Photo of DBR structures PR layer after developing. (d) Photo of AWG structure PR layer after developing.

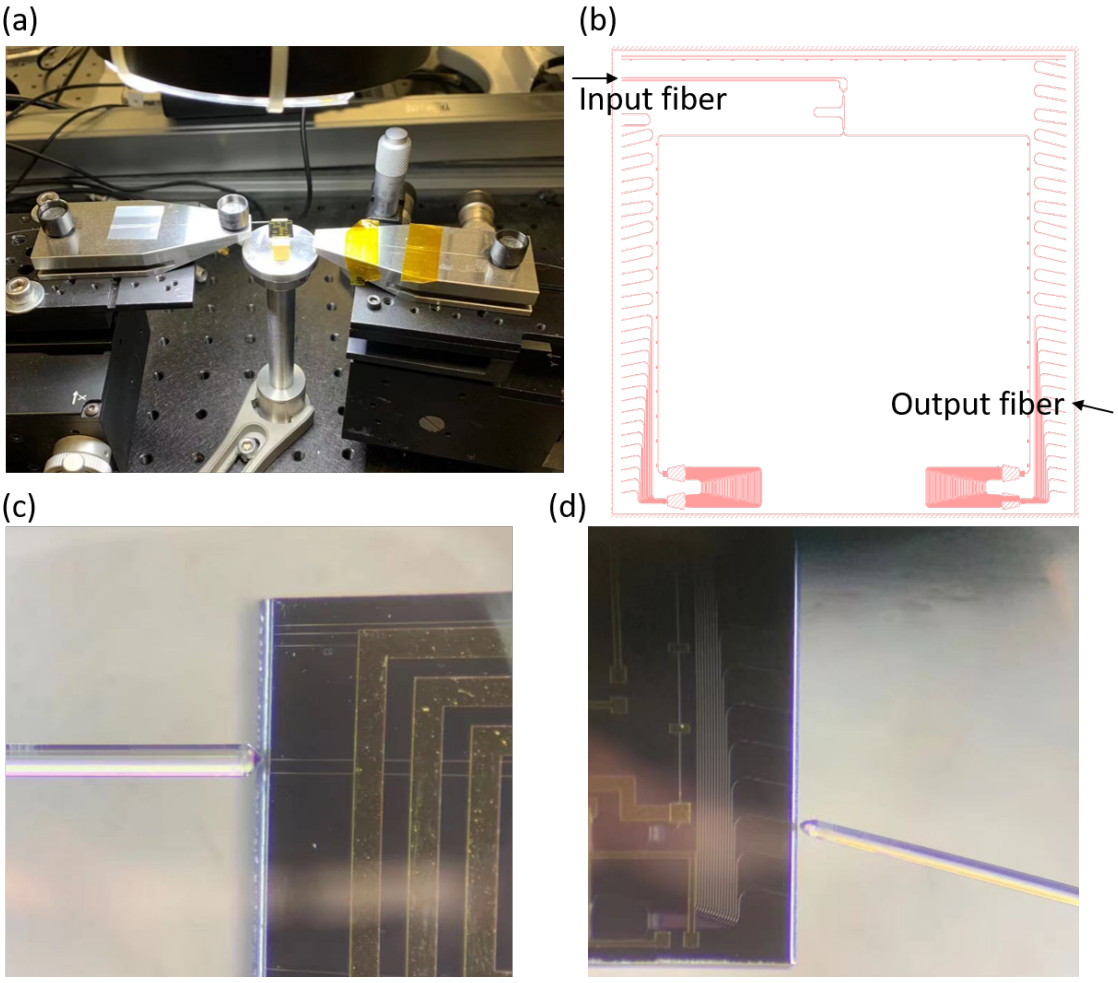


Figure 5.18. (a) Photo of WDM laser measurement setup (b) Schematic view of the measurement setup. (c) Photo of the input lens fiber. (d) Photo of the output lens fiber.

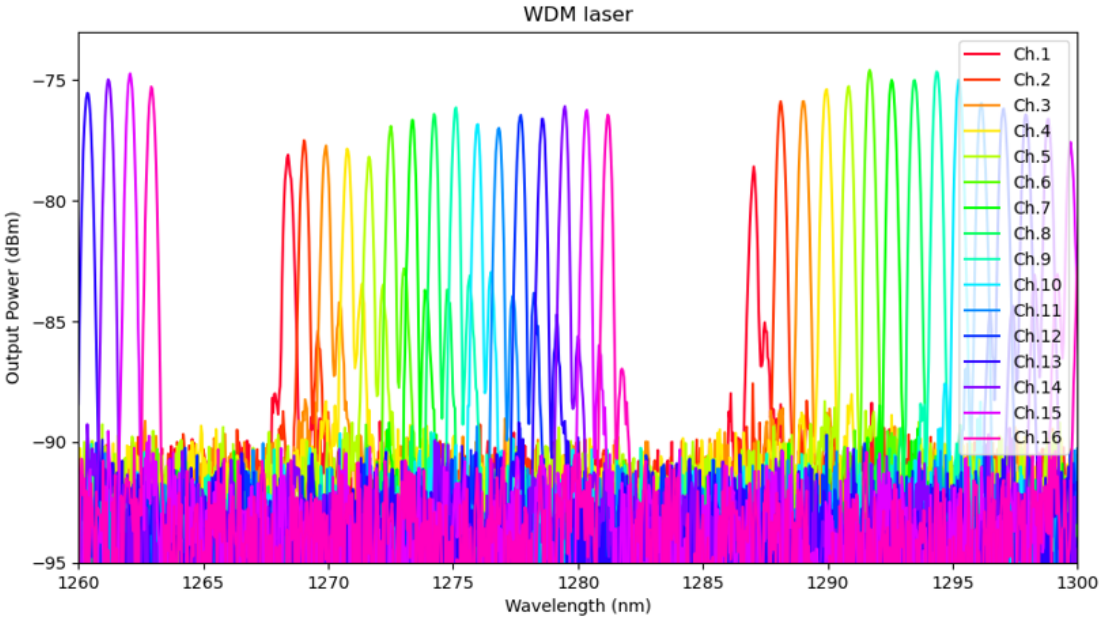


Figure 5.19. 16 channel AWG with the interleaver passband spectrum measured.

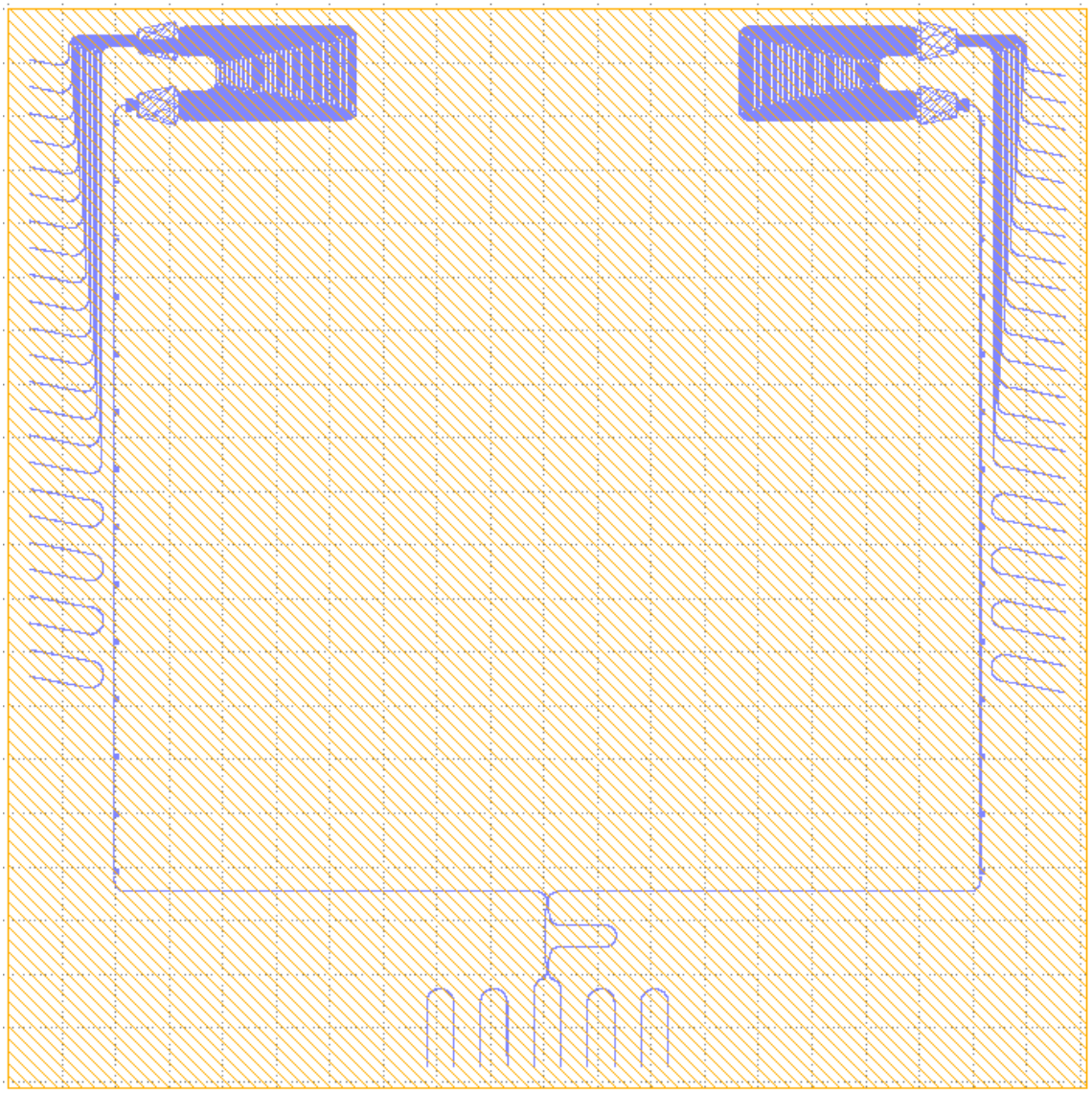

Figure 5.20. This is the layout of the second run of the WDM laser. The best AWG, interleaver and SGDBR are chosen. The input waveguides on the east side are pointed down based on FreedomPhotonics' requirements. The output waveguides are pointed to south and four loopback waveguides designed for alignment are added.

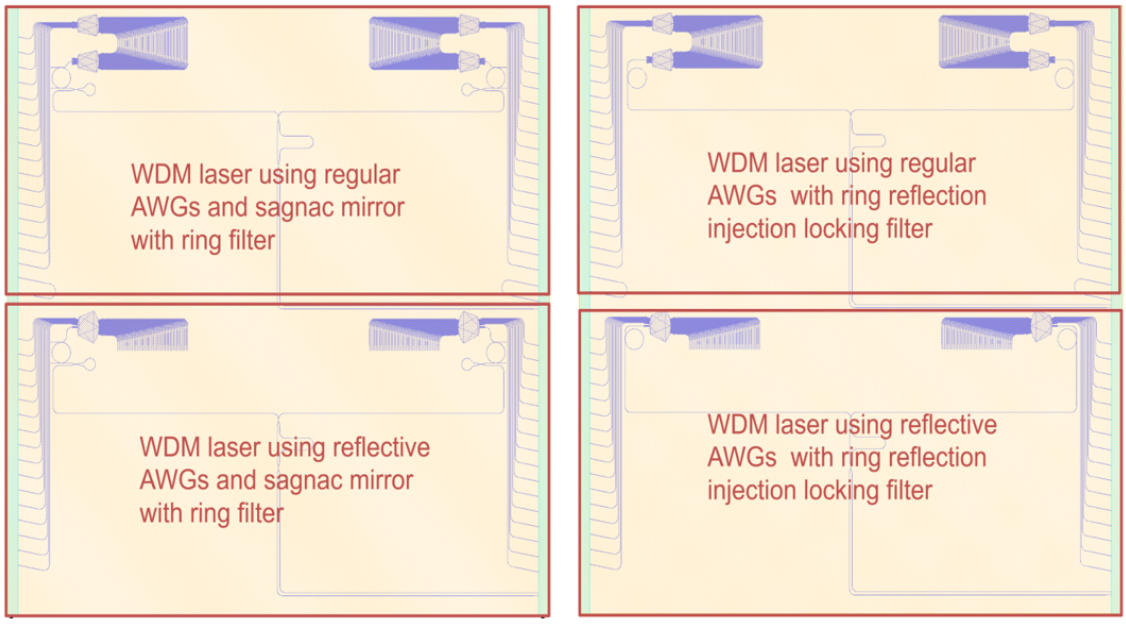


Figure 5.21. Four alternative WDM laser designs. All of them use reflectors with shorter cavity length compared with SGDBR.

# References


[1] C. A. Brackett. Dense wavelength division multiplexing networks: principles and applications. *IEEE Journal on Selected Areas in Communications*, 8(6):948–964, 1990.

[2] Meint K Smit. Progress in awg design and technology. In *Proceedings of 2005 IEEE/LEOS Workshop on Fibres and Optical Passive Components, 2005.*, pages 26–31. IEEE, 2005.

[3] R. N. Hall, G. E. Fenner, J. D. Kingsley, T. J. Soltys, and R. O. Carlson. Coherent light emission from gaas junctions. *Phys. Rev. Lett.*, 9:366–368, Nov 1962.

[4] B. Jalali and S. Fathpour. Silicon photonics. *Journal of Lightwave Technology*, 24(12):4600–4615, 2006.

[5] G. K. Celler and Sorin Cristoloveanu. Frontiers of silicon-on-insulator. *Journal of Applied Physics*, 93(9):4955–4978, 2003.

[6] Yurii Vlasov and Sharee McNab. Losses in single-mode silicon-on-insulator strip waveguides and bends. *Optics express*, 12:1622–31, 05 2004.

[7] K. Shang, S. Pathak, C. Qin, and S. J. B. Yoo. Low-loss compact silicon nitride arrayed waveguide gratings for photonic integrated circuits. *IEEE Photonics Journal*, 9(5):1–5, 2017.

[8] Katsunari Okamoto. *Fundamentals of optical waveguides*. Academic press, 2006.

[9] Koichi Maru, Tetsuya Mizumoto, and Hisato Uetsuka. Modeling of multi-input arrayed waveguide grating and its application to design of flat-passband response using cascaded mach–zehnder interferometers. *Journal of lightwave technology*, 25(2):544–555, 2007.

[10] Pascual Munoz, Daniel Pastor, and Jose Capmany. Modeling and design of arrayed waveguide gratings. *Journal of lightwave technology*, 20(4):661, 2002.

[11] C Dragone, CA Edwards, and RC Kistler. Integrated optics n* n multiplexer on silicon. *IEEE Photonics Technology Letters*, 3(10):896–899, 1991.

[12] Salman Naeem Khan, Daoxin Dai, Liu Liu, Lech Wosinski, and Sailing He. Optimal design for a flat-top awg demultiplexer by using a fast calculation method based on a gaussian beam approximation. *Optics Communications*, 262(2):175 – 179, 2006.

[13] David J Geisler, Nicolas K Fontaine, Ryan P Scott, Tingting He, Loukas Paraschis, Ori Gerstel, Jonathan P Heritage, and SJB Yoo. Bandwidth scalable, coherent transmitter based on the parallel synthesis of multiple spectral slices using optical arbitrary waveform generation. *Optics express*, 19(9):8242–8253, 2011.

[14] JBD Soole, MR Amersfoort, HP LeBlanc, NC Andreadakis, A Rajhel, C Caneau, R Bhat, MA Koza, C Youtsey, and Ilesanmi Adesida. Use of multimode interference couplers to broaden the passband of wavelength-dispersive integrated wdm filters. *IEEE Photonics Technology Letters*, 8(10):1340–1342, 1996.

[15] T Kitoh, Y Inoue, M Itoh, M Kotoku, and Y Hibino. Low chromatic-dispersion flat-top arrayed waveguide grating filter. *Electronics Letters*, 39(15):1116–1118, 2003.

[16] An Jun-Ming, Wu Yuan-Da, Li Jian, Li Jian-Guang, Wang Hong-Jie, Li Jun-Yi, and Hu Xiong-Wei. Fabrication of triplexers based on flattop soi awg. *Chinese Physics Letters*, 25(5):1717, 2008.

[17] K Takada, M Abe, T Shibata, and K Okamoto. 10-ghz-spaced 1010-channel tandem awg filter consisting of one primary and ten secondary awgs. *IEEE Photonics Technology Letters*, 13(6):577–578, 2001.

[18] L Grave De Peralta, AA Bernussi, S Frisbie, R Gale, and H Temkin. Reflective arrayed waveguide grating multiplexer. *IEEE Photonics Technology Letters*, 15(10):1398–1400, 2003.

[19] Daoxin Dai, Xin Fu, Yaocheng Shi, and Sailing He. Experimental demonstration of an ultracompact si-nanowire-based reflective arrayed-waveguide grating (de) multiplexer with photonic crystal reflectors. *Optics letters*, 35(15):2594–2596, 2010.

[20] Juan Fernández, Joan Felip, Bernardo Gargallo, José David Doménech, Daniel Pastor, Carlos Domínguez-Horna, and Pascual Muñoz. Reconfigurable reflective arrayed waveguide grating using optimization algorithms. *Optics Express*, 28(21):31446–31456, 2020.

[21] Tingting Lang, Jian-Jun He, Jing-Guo Kuang, and Sailing He. Birefringence compensated awg demultiplexer with angled star couplers. *Optics express*, 15(23):15022–15028, 2007.

[22] Yan Yang, Xiaonan Hu, Junfeng Song, Qing Fang, Mingbin Yu, Xiaoguang Tu, Guo-Qiang Lo, et al. Thermo-optically tunable silicon awg with above 600 ghz channel tunability. *IEEE Photonics Technology Letters*, 27(22):2351–2354, 2015.

[23] Chia-Ming Chang, Guilhem de Valicourt, S Chandrasekhar, and Po Dong. Differential microring modulators for intensity and phase modulation: Theory and experiments. *Journal of Lightwave Technology*, 35(15):3116–3124, 2017.

[24] Mike Davies, Narayan Srinivasa, Tsung-Han Lin, Gautham Chinya, Yongqiang Cao, Sri Harsha Choday, Georgios Dimou, Prasad Joshi, Nabil Imam, Shweta Jain, et al. Loihi: A neuromorphic manycore processor with on-chip learning. *Ieee Micro*, 38(1):82–99, 2018.

[25] David J Geisler, Nicolas K Fontaine, Ryan P Scott, Tingting He, Loukas Paraschis, Jonathan P Heritage, and SJB Yoo. 400-gb/s modulation-format-independent single-channel transmission with chromatic dispersion precompensation based on oawg. *IEEE Photonics Technology Letters*, 22(12):905–907, 2010.

[26] Jie Yang, Nicolas K Fontaine, Zhong Pan, Aytug O Karalar, Stevan S Djordjevic, Chunxin Yang, Wei Chen, Sai Chu, Brent E Little, and SJB Yoo. Continuously tunable, wavelength-selective buffering in optical packet switching networks. *IEEE Photonics Technology Letters*, 20(12):1030–1032, 2008.

[27] Junfeng Song, Q Fang, SH Tao, MB Yu, GQ Lo, and DL Kwong. Passive ring-assisted mach-zehnder interleaver on silicon-on-insulator. *Optics express*, 16(12):8359–8365, 2008.